

Spectral Energy Distributions of Southern Binary X-Ray Sources

JOHN M. DICKEY,¹ S. D. VRTILEK,² MICHAEL MCCOLLOUGH,² BRAM BOROSON,³ JOHN A. TOMSICK,⁴ CHARLES BAILYN,⁵
JAY M. BLANCHARD,^{6,1} AND CHARLOTTE JOHNSON³

¹*School of Natural Sciences, Private Bag 37, University of Tasmania, Hobart, TAS, 7001, Australia*

²*Harvard-Smithsonian Center for Astrophysics, 60 Garden Street, Cambridge, MA 02138, USA*

³*Dept. of Physics and Astronomy, University of South Carolina, 712 Main St., Columbia, SC 29208 USA*

⁴*Space Sciences Laboratory, University of California, Berkeley, 7 Gauss Way, Berkeley, CA 94720-7450, USA*

⁵*Department of Astronomy, Yale University, PO Box 208101, New Haven, CT 06520-8101, USA*

⁶*National Radio Astronomy Observatory, P.O. Box O, 1003 Lopezville Rd., Socorro, NM 87801-0387, USA*

ABSTRACT

The rapid variability of X-ray binaries produces a wide range of X-ray states that are linked to activity across the electromagnetic spectrum. It is particularly challenging to study a sample of sources large enough to include all types in their various states, and to cover the full range of frequencies that show flux density variations. Simultaneous observations with many telescopes are necessary. In this project we monitor 48 X-ray binaries with seven telescopes across the electromagnetic spectrum from 5×10^9 Hz to 10^{19} Hz, including ground-based radio, IR, and optical observatories and five instruments on two spacecraft over a one-week period. We construct spectral energy distributions and matching X-ray color-intensity diagrams for 20 sources that have the most extensive detections. Our observations are consistent with several models of expected behavior proposed for the different classes: we detect no significant radio emission from pulsars or atoll sources, but we do detect radio emission from Z sources in the normal or horizontal branch, and from black holes in the high/soft, low/hard and quiescent states. The survey data provide useful constraints for more detailed models predicting behavior from the different classes of sources.

Keywords: Stellar remnants: compact objects, stellar remnants: ejecta, High Energy Astrophysics: black holes, Binary stars

1. INTRODUCTION

Many of the brightest X-ray sources in the sky are mass-exchange binary stars in which a collapsed object accretes material from its main sequence or red giant companion. X-ray binaries (XRBs) generally show evidence for an accretion disk; if the collapsed object is a neutron star or black hole the inner region of the disk is hot enough that the black-body peak can be at energies ($h\nu > 1$ keV), but other emission processes may dominate. Often the accretion disk powers a jet of relativistic electrons and magnetic field that emits synchrotron radiation and/or inverse Compton scatters lower frequency photons into the X-ray and γ -ray bands. Comptonization can also be due to scattering by electrons in the corona of the accretion disk, a jet is not necessary. XRBs have been called micro-quasars (Mirabel 1993) because they are similar to active galactic nuclei in both their structure and emission processes, but with masses, luminosities, and dynamical time scales 10^6 to 10^9 times smaller. XRBs are among the few objects that are bright across the spectrum from cm-wave radio to MeV γ -rays. Rapid variations in their emission spectra show the effects of different states linked to accretion rate changes. These can happen much faster in micro-quasars than in active galactic nuclei, typically the time scale is proportional to the collapsed object mass. Monitoring XRBs with telescopes to cover all wavelengths may reveal how the accretion disk drives the jet, and the structural connection between them. For example, most jet theories invoke a poloidal magnetic field arising from the accretion disk that collimates the jet flow. Variations in accretion rate on time scales of days to weeks are common in XRBs ; similar variations take much longer in active galactic nuclei.

Well-studied XRBs can be classified according to the properties of the collapsed object and its magnetic field (e.g. Migliari & Fender 2006). In black hole (BH) systems the compact object is a stellar mass black hole, the companion

star can have either high or low mass. Those with low mass companions are sometimes referred to as soft X-ray transients (SXTs). SXTs can increase by factors of 100 to 10,000 in brightness at both X-ray and optical wavelengths. These variations are due to dramatic changes in mass accretion rate from the companion to the BH. While few SXT's are persistent, i.e. continuously active, most systems with high mass companions are persistent.

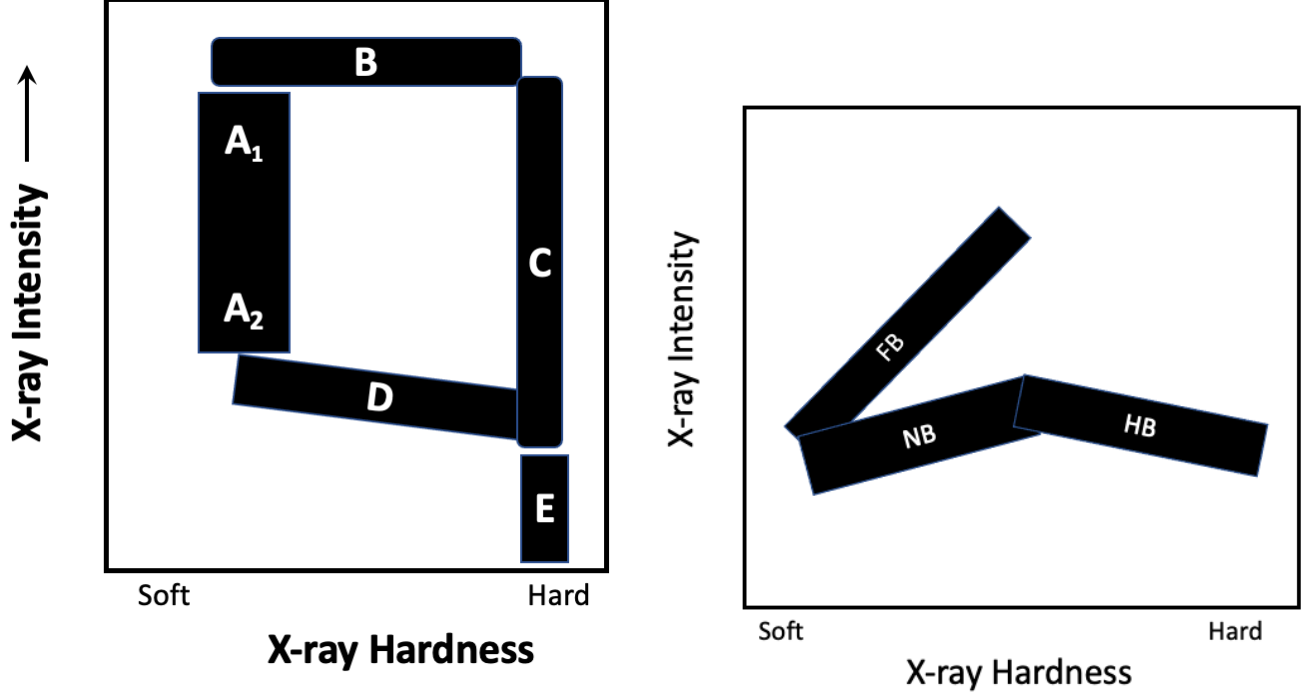


Figure 1. Schematics illustrating the characteristic behavior of BH (left panel) and Z-type (right-panel) XRBs on plots of X-ray color vs. intensity (CI). The various states (labeled A-E for clarity on the left panel) are described in Section 1.

Black Holes: BHs have very distinctive patterns in X-ray color-color (CC) and color-intensity (CI) diagrams (e.g. [Remillard & McClintock 2006](#)). Fig. 1, left panel, presents a schematic with black rectangles labeled A-E to indicate the different BH states as defined here:

- A1 the high/soft state. In this state the X-rays are dominated by thermal emission. There are relatively large jets, typically hundreds of AU in size, that are optically thin, highly relativistic and transient on short time scales. [Remillard & McClintock \(2006\)](#) call this the Steep Power Law (SPL), [Belloni et al. \(2005\)](#) call it the Soft-Intermediate State (SIMS).
- A2 the soft/low state. In this state the radio jet is quenched and the accretion disk dominates the emission at all wavelengths (e.g. [Fender et al. 1999](#)).
- B the bright, intermediate state. The source shows superluminal ejection and a radio flare. The X-rays indicate a hot corona in addition to the accretion disk.
- C the hard/low state. The X-ray luminosity is high, greater than 10^{-2} times the Eddington luminosity. There is a hot corona, and a persistent, flat-spectrum radio source, typically in the mJy range, whose emission extends to the IR and optical. The radio source is compact, roughly 10 AU in size. The radio, IR, and X-rays show correlation in their variability. The X-ray spectrum indicates a reflection component.
- D the faint, intermediate state. Here there is no radio emission, the X-rays indicate a hot corona in addition to the accretion disk.

- E the quiescent state. The source includes a hot corona plus a black body component that dominates the ultra-violet and optical. There is a persistent, flat-spectrum, compact radio source at the μJy level (e.g. Kalemci et al. 2005; Plotkin et al. 2013; Gallo et al. 2015, 2018; Shaw et al. 2021).

In the quiescent state, the luminosity of a BH XRB is lower than that of a neutron star XRB in quiescence, because the BH has no surface (Garcia et al. 2001)

Z-sources: The compact object is a neutron star with a low-mass companion, in which the mass accretion is typically more than 50 percent of the Eddington limit. Z-sources are named for the shape they form on X-ray CC diagram as a result of changes in both spectral and timing properties. The schematic in Fig. 1, right panel, shows the three nominal states in a CI diagram: Horizontal Branch (HB, right side); Normal Branch (NB, middle); Flaring Branch (FB, upper left). Radio emission is strongest in the HB, decreases during the NB, and is usually not detectable during the FB. In the HB state there is a steady radio jet that changes into a transient compact radio jet in the NB (e.g. Migliari et al. 2007). The slope of the HB is much steeper in “Cyg X-2-like” Z-track sources than in “Sco X-1-like” sources and the flaring branch in Sco X-1-like sources goes to much higher intensities than in Cyg X-2-like sources. Several papers suggest that the flaring branch in Sco X-1-like sources is a combination of unstable burning and an increase of \dot{M} , the mass accretion rate, which makes flaring much stronger; whereas the flaring branch in the Cyg X-2-like sources is associated with a release of energy on the neutron star consistent with unstable nuclear burning. (Balucinska-Church et al. 2010; Church et al. 2012). Fig. 1 shows a generic CI diagram for Z-sources that is roughly consistent for both types: both NB and FB usually increase in intensity and hardness from the node between the FB and the NB. The HB decreases in intensity but increases in hardness from the node between the HB and the NB. Z-sources typically have higher accretion rates than Atolls.

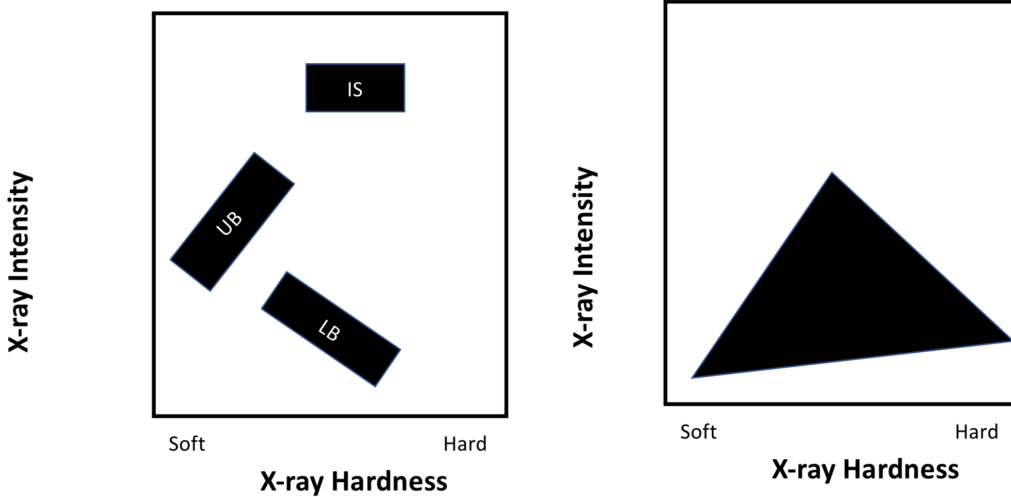


Figure 2. Schematics illustrating the characteristic behavior of Atoll (left panel) and Pulsar (right panel) XRBs on plots of X-ray color vs. intensity (CI). The various states are described in Section 1.

Atolls: The compact object is a neutron star and the companion star is low-mass and the mass accretion is generally less than ten percent of Eddington. Atoll sources are named for the shapes they occasionally form in X-ray CC and CI diagrams (Fig. 2, left panel). They fall into several spectral states: a hard, high luminosity ‘island’ (IS) or a soft, lower luminosity ‘banana’; the banana branch is subdivided into upper banana (UB) and lower banana (LB) based on changes in both spectral and timing properties. The transition between these states is rapid and not covered well by observations. A subset of atolls are referred to as bursters: these increase by factors of 10 to 100 in X-ray luminosity due to thermonuclear flashes on the surface of the neutron star. Atolls typically have lower accretion rates than Z-sources. It has been shown that some Z and Atoll sources can morph into each other with major changes in mass accretion rate (Homan et al. 2010).

Pulsars: The compact object is a neutron star and the companion can be either high or low-mass. The neutron star is highly magnetized ($|B| > 10^{12}$ G); gas accreted from the companion is guided by the neutron star's magnetic field onto the magnetic poles producing two or more localized X-ray hot spots. As the neutron star rotates the X-rays appear to pulse as the spots rotate in and out of view. This X-ray emission is generally not associated with any pulsed radio emission but some millisecond pulsars do display radio pulses (rotationally powered) although with a significant phase offset between X-ray and radio pulses (Papitto et al. 2013; Guillot et al. 2019). In X-ray CC and CI diagrams they cluster towards hard colors with little or no dependence on intensity (Fig. 2, right panel). No resolved jets have been observed but van den Eijnden et al. (2018) detect evolving radio emission from several X-ray pulsars.

This project constitutes an extensive program to obtain spectral energy distributions (SEDs) from the radio through the X-rays for a representative selection of accreting binaries. The impetus for such a survey was the simultaneous availability of multiple space observatories in conjunction with ground-based radio and optical facilities in combinations that allowed us to span the full range of available wavelengths efficiently. SEDs are often obtained based on target of opportunity telescope observations of a given source in a specific state. Such campaigns have revealed a lot about the time evolution of emission in individual sources (e.g. McClintock et al. 2001; Vrtillek et al. 2001; Sivakoff et al. 2016). Here we obtained observing time on seven telescopes for a large sample of sources over a one week interval: this allowed us to trace patterns of behavior among different categories of XRBs.

The telescopes and observations are described in section 2. The results for each source are presented in section 3. In section 4 we interpret our results in the context of the characteristic patterns of behavior in color-intensity diagrams.

2. OBSERVATIONS

Our coordinated observing program took place from June 29-July 6, 2007 (MJD 54280-54287). Sources were selected from the low-mass X-ray binary (LMXB) and high-mass X-ray binary (HMXB) catalogs of Liu et al. (2001, 2006). We include sources that have known optical and/or near-IR counterparts and are at least $5''$ away from objects of similar brightness; we exclude Globular Clusters. Since the ground-based telescopes are in the Southern Hemisphere, we include only sources south of $\delta = +12^\circ$. The resulting sample has 48 sources including 11 black holes (BHs), 8 Z-sources, 19 Atoll sources; and 10 X-ray Pulsars. Seven telescopes were coordinated to cover the spectrum from radio at 4.8 GHz to X-rays at 50 keV. These include the Australia Telescope Compact Array (ATCA) at 4.8 and 8.64 GHz, the Small and Moderate Aperture Research Telescope System (SMARTS) in the near-IR K, H, and J bands and in the optical V band, the UV-Optical Telescope (UVOT) aboard the Neil Gehrels Swift Observatory (Swift) in the optical V and B bands and the ultraviolet U, UVW1, UVM2 and UVW2 bands, the Swift X-ray Telescope (XRT) from 0.5 to 10 keV, the Swift Burst Alert Telescope (BAT) from 5 to 50 keV, the Rossi X-ray Timing Explorer (RXTE) All-sky monitor (ASM) from 1.3 to 12 keV, and the RXTE Proportional Counter Array (PCA) from 2 to 20 keV. A summary spreadsheet listing the XRB names and positions, the telescopes, and the observations and detections for each band is shown on Table 1. Another class of interacting binaries, symbiotic stars, were observed as part of this project, but only at radio frequencies. Results for the symbiotics are described in Dickey et al. (2021), but GX 1+4, the prototype symbiotic with a neutron star companion, is included in this paper along with the pulsars.

2.1. Radio Observations

The data were taken with the Australia Telescope Compact Array in the 6C configuration, that has 15 East-West baselines with lengths from 150 m to 6 km, giving angular resolution of about $2''$ at 4.8 GHz and $1.1''$ at 8.64 GHz. These two frequencies were observed simultaneously with total bandwidth 128 MHz for each, of which the central 96 MHz was used to avoid filter edge-effects (correlator configuration full_128_2).

Flux densities were calibrated by daily observations of 1934-638, the absolute flux standard for southern hemisphere observations at cm wavelengths. The standard calibration procedure using the MIRIAD software package was followed (Sault et al. 2004).

As described in Dickey et al. (2021), we did not attempt to map every source. The standard approach of aperture synthesis imaging is not well suited to monitoring a rapidly varying source, as the aperture or u,v plane, which is the Fourier Transform of the image or sky plane, is not well sampled until Earth rotation has caused the baselines between telescopes to follow tracks that cover a large fraction of the aperture. This typically takes 12 hours. For this project we could spend only a few minutes of telescope time on each source each day, and the sources might change their flux densities from day to day, or even hour to hour. Analysis of short scans on each XRB taken on the first three days was done using the complex fringe visibility function as measured at each u,v point (baseline and time). These visibilities

Source	RA J2000	Dec J2000	ATCA		SMARTS			V_θ	SWIFT UVOT				SWIFT		RXTE		SWIFT	
			C	X	K	H	J		V	B	U	UVW1	UVM2	UVW2	XRT	ASM	PCA	BAT
Black Holes (11)																		
LMC X-3 ^a	05:38:56.63	-64:05:03.3	-	-	+	+	+	-	+	...
LMC X-1	05:39:38.83	-69:44:35.5	-	-	+
XTE J1550-564	15:50:58.65	-56:28:35.3	-	-	-	-	-
4U 1630-47	16:34:01.61	-47:23:34.8	-	-	-	-	-
GRO J1655-40	16:54:00.14	-39:50:44.9	-	-	+	+	-
GX 339-4 ^a	17:02:49.38	-48:47:23.2	+	+	+	+	+	+	+	+	+	+	+	-	+	+
1E 1740.7-2942 ^a	17:43:54.83	-29:44:42.6	-	-	-	-	+	+
GRS 1758-25 ^g	18:01:12.40	-25:44:36.1	-	-	-	+	+	...	+
V4641 Sgr	18:19:21.63	-25:24:25.8	-	-	+	+	-
GRS1915+105 ^g	19:15:11.56	+10:56:44.9	+	+	+	...
4U 1957+11 ^a	19:59:24.01	+11:42:29.9	-	-	+	+	+	+	+
Z Sources (8)																		
LMC X-2	05:20:28.04	-71:57:53.3	-	-	+	...	+
Cir X-1 ^a	15:20:40.85	-57:10:00.1	+	+	+	...	+	+	-	-	+	-	...	+
Sco X-1 ^a	16:19:55.07	-15:38:25.0	+	+	+	+	...
GX 340+0	16:45:47.70	-45:36:40.0	-	-	+
XTE J1701-462 ^a	17:00:58.46	-46:11:08.6	-	-	+	-	+	+	+	+
GX 349+2 ^a	17:05:44.49	-36:25:23.0	-	-	+	+	+	+	+
GX 5-1	18:01:09.73	-25:04:44.1	+	+	+	+
GX 17+2 ^a	18:16:01.39	-14:02:10.6	+	+	+	-	+	+	...	+

Source	RA J2000	Dec J2000	ATCA C	ATCA X	SMARTS			V	B	SWIFT UVOT			SWIFT XRT	RXTE ASM	RXTE PCA	SWIFT BAT
AtoII Sources (18)					K	H	J	V		U	UVW1	UVN2	UVW2			
EXO 0748-676 ^a	07:48:33.71	-67:45:07.7	-	-	+	+	+
2S 0921-630	09:22:34.68	-63:17:41.4	-	-	-
4U 1254-690 ^a	12:57:37.15	-69:17:19.0	-	-	-	+	+	+	+
Cen X-4	14:58:21.93	-31:40:07.5	-	-	+	+	+	+	-
4U 1543-624	15:47:54.6	-62:34:06	-	-	+	+	+
4U 1556-60	16:01:02.30	-60:44:18.0	-	-	+
4U 1608-52 ^a	16:12:43.0	-52:25:23	-	-	-	-	...	+	-	-	...	+	+	+
4U 1636-536 ^a	16:40:55.60	-53:45:05.0	-	-	+	+	+	+	+
MXB 1658-298	17:02:06.54	-29:56:44.1	-	-	-	+	+
4U 1702-429	17:06:15.31	-43:02:08.7	-	-	+
4U 1705-44 ^a	17:08:54.47	-44:06:07.4	-	-	+	+	+
GX 9+9 ^a	17:31:44.17	-16:57:40.9	-	-	+	+	+	...	+	+	+
GX 354+0 ^a	17:31:57.73	-33:50:02.5	-	+	-	...	+	...	+
4U 1735-444 ^a	17:38:58.3	-44:27:00	-	-	+	+	+	...	+	+	+
GX 3+1	17:47:56.00	-26:33:49.0	-	-	+
GX 9+1	18:01:32.30	-20:31:44.0	-	-	+
GX 13+1	18:14:31.55	-17:09:26.7	-	-	+
Aql X-1 ^a	19:11:16.06	+00:35:05.9	+	+	+	+	...

Source	RA J2000	Dec J2000	ATCA			SMARTS			V	SWIFT UVOT				SWIFT XRT	RXTE ASM	RXTE PCA	SWIFT BAT
			C	X	K	H	J	V		B	U	UVW1	UVM2				
Pulsars (11)																	
SMC X-3	00:52:05.63	-72:26:04.2	-	-	+	+	-
SMC X-1 ^a	01:17:05.14	-73:26:36.0	-	-	+	+	+	+	+	...	+
Vela X-1	09:02:06.86	-40:33:16.9	-	-	+
Cen X-3	11:21:15.09	-60:37:25.6	-	-	+	+	+
GX 301-2	12:26:37.56	-62:46:13.3	-	-	+	+	+
4U 1538-522	15:42:23.36	-52:23:09.6	-	-	+	+	+
4U 1700-37 ^b	17:03:56.77	-37:50:38.9	-	-	+
GX 1+4	17:32:02.15	-24:44:44.1	-	-	+	+	-
Swift J1756.9-2508	17:56:57.35	-25:06:27.8	-	-	-	-	-
4U 1822-371 ^a	18:25:46.82	-37:06:18.5	-	-	+	+	+	+
4U 1907+097 ^a	19:09:37.14	+09:49:55.3	+	-	+	+	+

Table 1. XRBs observed in this experiment. Observations are indicated by + for detections, – for upper limits, ... indicates the object was not observed by the telescope indicated. Positions are provided by Simbad (simbad.cds.unistra.fr), mostly measured by Gaia (eDR3 [Bailer-Jones et al. 2021](#)) in ICRS coordinates.

Footnote ^a indicates sources with sufficient frequency ranges to analyse the spectral energy distribution (SED) in section 3.

^b While pulsations have not been detected, the position of 4U 1700-37 in color-color-intensity diagrams locates it as a pulsar ([Vrtilek & Boroson 2013](#); [Gopalan et al. 2015](#); [de Beurs et al. 2022](#)).

are vector-added by the MYRIAD task UVFLUX to determine the flux density of a point source at the phase center (the real part of the vector sum), and the rms error on the flux density. Sources that were not detected on any of the first three days of observations were not reobserved, upper limit flux densities are in most cases between 2 and 3 mJy at both frequencies. Starting on MJD 54284 (3 July 2007) we concentrated on the sources that showed detections or tentative detections, i.e. with flux density above about 1.5 mJy. For these detected sources, combining the data from all days gave sufficient u,v coverage for mapping and cleaning. We then fitted two dimensional Gaussians to each source. Table 2 gives the Gaussian parameters for each detected source at 8.64 and 4.80 GHz, and upper limits for the non-detections.

The source that shows by far the strongest variation from day to day during the observation is Sco X-1, with an increase from about 1 to 67 mJy between 30 June and 1 July (MJD 54281 - 54282), then back down to about 8 mJy on 4 July (MJD 54285) before increasing again to 19 mJy on 5 July (MJD 54286), as shown on figure 3. The radio variability of Sco X-1 has been studied by Fomalont et al. (2001). Cir X-1 also shows significant variations at 8.64 and 4.8 GHz, as shown on table 2. In this case the source is much weaker, it increases from about 1 mJy to over 6 mJy at 8.64 GHz from 29 June to 1 July (MJD 54280 - 54282), then drops below the detection limit (~ 1 mJy) from 3 July on (MJD > 54283).

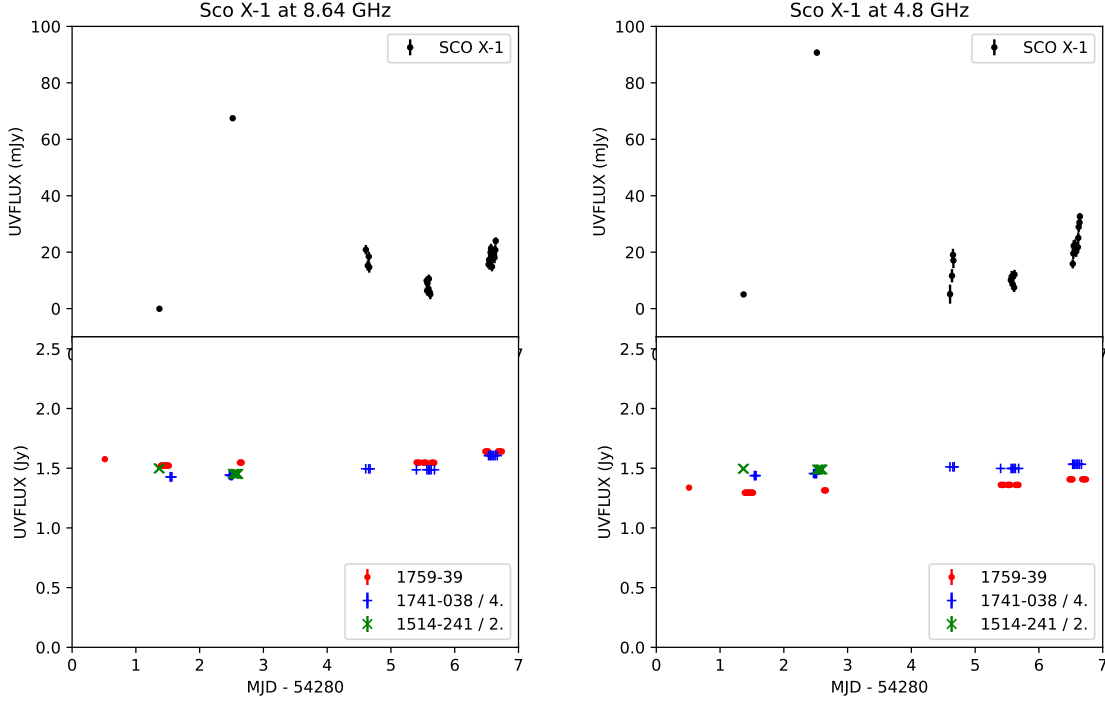


Figure 3. The variation in flux density of Sco X-1 measured at 8.64 GHz (left panel) and at 4.8 GHz (right panel). Error bars represent the errors on the means of the 10 second scans in each observation, they are mostly smaller than the markers. Measurements of three gain calibrators, 1759-39, 1741-038 and 1514-241, that were observed at nearly the same time as Sco X-1, are shown for comparison in the lower panels. Conveniently, their fluxes are very nearly in ratio 1:4:2, so dividing the measured fluxes for 1741-038 by four and those of 1514-241 by two puts them all on the same scale. The standard deviations of the calibrator fluxes at 8.64 GHz are 2.9% of the mean for 1759-39, 4.6% of the mean for 1741-038, and 1.4% of the mean for 1514-241. Thus the overall calibration errors due to gain variations are very likely less than 5%.

Table 2. Radio Frequency Detections and Upper Limits

Source	Dwell	Freq	S_{peak}^a	RA	Dec	MJD	S_{int}^b	Diam ^c
	sec	GHz	mJy/beam	J2000	J2000		mJy	"
Black Holes								
LMC X-3	590	8640	< 0.3					
LMC X-3	590	4800	< 0.3					
LMC X-1	1080	8640	< 18 ^d					
LMC X-1	1080	4800	< 6.3 ^d					
XTE J1550-564	527	8640	< 0.3					
XTE J1550-564	527	8640	< 0.4					
4U 1630-47	510	8640	< 0.7					
4U 1630-47	510	4800	< 2.0					
GRO J1655-40	823	8640	< 1.5					
GRO J1655-40	823	4800	< 0.6					
GX 339-4	1923	8640	1.03±0.09	17:02:49.38	-48:47:23.2	all	1.02±0.14	<4
GX 339-4	1923	4800	1.57±0.12	17:02:49.38	-48:47:22.8	all	1.59±0.17	<5
1E 1740.7-2942	1189	8640	<0.4					
1E 1740.7-2942	1189	4800	<2.1					
GRS 1758-258	630	8640	<0.2					
GRS 1758-258	630	4800	<0.3					
V4641 Sgr	630	8640	<0.5					
V4641 Sgr	630	4800	<0.2					
Z Sources								
LMC X-2	450	8640	<0.2					
LMC X-2	450	4800	<0.4					
Cir X-1	1630	8640	2.1±0.5	15:20:40.93	-57:09:59.9	all	6.7±3.4	<5
Cir X-1	1630	4800	3.5±0.5	15:20:40.83	-57:10:00.0	all	6.7±1.9	<5
Cir X-1	660	8640	1.0 ± 0.32	54279.3
Cir X-1	450	8640	22.5 ± 2.8	54280.2
Cir X-1	1500	8640	12.6 ± 0.4	54281.2
Cir X-1	690	8640	1.2 ± 0.5	54283.5
Cir X-1	180	8640	0.3 ± 0.6	54284.5
Cir X-1	330	8640	1.3 ± 0.4	54285.4
Cir X-1	660	4800	2.5 ± 0.5	54279.3
Cir X-1	450	4800	22.2 ± 1.0	54280.2
Cir X-1	1500	4800	14.3 ± 0.4	54281.2
Cir X-1	690	4800	2.4 ± 0.6	54283.5
Cir X-1	180	4800	1.9 ± 0.6	54284.5
Cir X-1	330	4800	1.0 ± 0.5	54285.4
Sco X-1 ^e	1020	8640	11.96±2.31	16:19:55.06	-15:38:25.9	all	13.86±12.01	<4
Sco X-1 ^e	1020	4800	15.95±0.98	16:19:55.07	-15:38:25.4	all	19.88±1.77	<9

Table 2 continued on next page

Table 2 (*continued*)

Source	Dwell	Freq	S_{peak}^a	RA	Dec	MJD	S_{int}^b	Diam ^c
	sec	GHz	mJy/beam	J2000	J2000		mJy	"
Sco X-1	540	8640	<1.5	54280.4
Sco X-1	450	8640	67.5 ± 1.1	54281.5
Sco X-1	600	8640	17.3 ± 1.2	54283.6
Sco X-1	210	8640	7.7 ± 0.6	54284.6
Sco X-1	360	8640	19.1 ± 0.6	54285.6
Sco X-1	540	4800	5.0 ± 0.6	54280.4
Sco X-1	450	4800	90.7 ± 1.8	54281.5
Sco X-1	600	4800	13.2 ± 1.5	54283.6
Sco X-1	210	4800	10.2 ± 0.7	54284.6
Sco X-1	360	4800	24.2 ± 0.6	54285.6
GX 340+0	527	8640	<1.4
GX 340+0	527	4800	<1.7
XTE J1701-462	1073	8640	<0.4
XTE J1701-462	1073	4800	<0.5
GX 349+2	920	8640	<0.3
GX 349+2	920	4800	<0.4
GX 5-1	760	8640	0.94 ± 0.08	18:01:08.22	-25:04:42.4	all	0.95 ± 0.90	<11
GX 5-1	760	4800	1.22 ± 0.21	18:01:08.22	-25:04:43.1	all	1.67 ± 0.44	<8
GX 17+2	2123	8640	0.78 ± 0.07	18:16:01.38	-14:02:11.0	all	0.89 ± 0.35	<6
GX 17+2	2123	4800	1.24 ± 0.14	18:16:01.39	-14:02:11.7	all	1.36 ± 0.23	4
Atoll Sources								
EXO 0748-676	1160	8640	<0.6
EXO 0748-676	1160	4800	<1.0
2S 0921-630	510	8640	<0.4
2S 0921-630	510	4800	<1.2
4U 1254-690	1017	8640	<0.6
4U 1254-690	1017	4800	<0.6
Cen X-4	330	8640	<0.3
Cen X-4	330	4800	<0.3
4U 1543-624	660	8640	<0.5
4U 1543-624	660	4800	<0.5
4U 1556-60	527	8640	<0.4
4U 1556-60	527	4800	<0.6
4U 1608-52	920	8640	<0.4
4U 1608-52	920	4800	<0.4
4U 1636-536	987	8640	<0.4
4U 1636-536	987	4800	<0.4
MXB 1658-298	310	8640	<0.3
MXB 1658-298	310	4800	<0.3
4U 1702-429	607	8640	<0.4

Table 2 *continued on next page*

Table 2 (*continued*)

Source	Dwell	Freq	S_{peak}^a	RA	Dec	MJD	S_{int}^b	Diam ^c
	sec	GHz	mJy/beam	J2000	J2000		mJy	"
4U 1702-429	607	4800	<0.4
4U 1705-44	570	8640	<0.3
4U 1705-44	570	4800	<0.4
GX 9+9	1577	8640	<0.4
GX 9+9	1577	4800	<0.4
GX 354+0	881	8640	0.61±0.09	17:31:57.73	-33:50:00.4	all	0.69±0.15	<6
GX 354+0	881	4800	<0.5
4U 1735-444	1020	8640	<0.4
4U 1735-444	1020	4800	<0.5
GX 3+1	340	8640	<0.9
GX 3+1	340	4800	<0.5
GX 9+1	440	8640	<0.8
GX 9+1	440	4800	<0.6
Swift J1756.9-2508	1400	8640	<0.4
Swift J1756.9-2508	1400	4800	<1.7
GX 13+1	310	8640	<0.7
GX 13+1	310	4800	<3.6
4U 1822-371	310	8640	<0.2
4U 1822-371	310	4800	<0.6
Pulsars								
SMC X-3	464	8640	<0.9
SMC X-3	464	4800	<2.1
SMC X-1	460	8640	<0.4
SMC X-1	460	4800	<0.4
Vela X-1	490	8640	<0.3
Vela X-1	490	4800	<0.3
Cen X-3	520	8640	<0.3
Cen X-3	520	4800	<0.3
GX 301-2	537	8640	<0.7
GX 301-2	537	4800	<1.0
4U 1538-52	510	8640	<0.3
4U 1538-52	510	4800	<0.5
4U 1700-37	540	8640	<0.5
4U 1700-37	540	4800	<1.1
GX 1+4	197	8640	<0.7
GX 1+4	197	4800	<1.9

Table 2 *continued on next page*

Table 2 (*continued*)

Source	Dwell	Freq	S_{peak}^a	RA	Dec	MJD	S_{int}^b	Diam ^c
	sec	GHz	mJy/beam	J2000	J2000		mJy	"

^a S_{peak} is the peak brightness of the fitted Gaussian.

^b S_{int} is the integrated flux density of the fitted Gaussian.

^c Diam is the full width to half maximum of the fitted Gaussian; these are mostly upper limits.

^d Confused by nearby sources in field.

^e See Fig. 3.

2.2. Infrared and Optical Observations

Observations in the near infrared and optical bands were made with the SMARTS (Small and Moderate Aperture Research Telescope System) 1.3m telescope at CTIO and the ANDICAM-IR instrument with a NICMOS 4 detector. The near infra-red channel (NIR) has pixel scale $0.275''$ and field of view (FoV) $2.4'$, while the optical channel has pixel scale $0.372''$ and FoV $6'$ (Muzerolle et al. 2019). The infrared observations were first flat-fielded using flat-field exposures taken one per night at J, H, and/or K band. These are used to flag bad pixels and to determine a scale factor for each good pixel that is applied to every exposure before aligning all exposures to a common center. All exposures for each night are then combined by taking the median for each pixel. A single frame for each night is saved, and an overall median image is computed for each source, an example is shown in figure 4. Coordinates and magnitudes are taken from comparison with star images in each band from the 2MASS survey (Skrutskie et al 2006). Simple geometric scale and rotation parameters were derived using the KOORDS utility in the KARMA package (Gooch 1996). Comparison of the derived star centroid positions with those in the 2MASS catalog gives an estimate for the precision of the coordinates of better than $1''$ in most cases. Magnitudes and fluxes for each source observed in the IR and optical are given on Table 3. In a few cases, source positions in the 2MASS catalog differ from those in the Gaia eDR3 (Gaia Collaboration et al. 2018) catalog (listed on Table 1 columns 2 and 3) by more than $3''$. These are noted in the footnotes to Table 3.

Fig. Set 4. SMARTS K,H,J band images

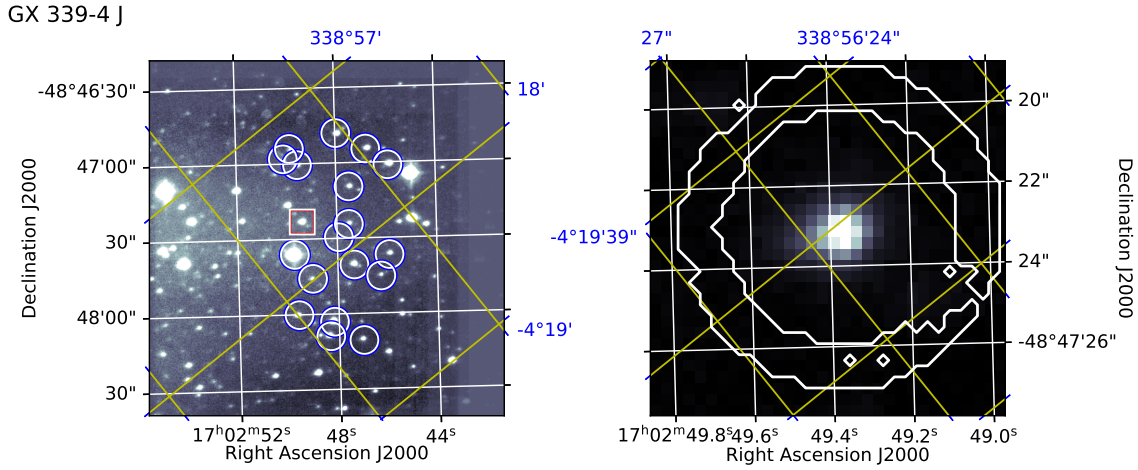


Figure 4. SMARTS Andicam image of the field of GX 339-4 at J band. On the left is the full field image, with photometric reference stars indicated by blue circles and the X-ray source by a red square with side length 32 pixels= $8.8''$. On the right is a blow-up of the area inside the red square. ICRF coordinates are indicated in black with white grid lines. Galactic coordinates are shown in blue, with yellow grid lines. The source is fitted by a two dimensional Gaussian after subtracting the background using a bi-linear function fitted to pixels inside the annulus indicated by the white contour. Confusing stars or other pixels more than 1.5 sigma above the mean in the annulus are dropped before fitting, as indicated by the ragged boundaries of the white contour. The complete figure set (37 images) is available in the online journal.

In each field, 50 comparison stars from the 2MASS point source catalog (Cutri et al. 2003)¹ are considered, and those that are unconfused are used to calibrate the photometry of the program sources. Two dimensional Gaussians are fitted to the star images, and their integrals are assumed to be proportional to the flux in the band. The catalog magnitudes are fitted by a linear function of the logarithm of the flux, and the result is used to convert the program source flux to magnitude. An example of the flux vs. magnitude calibration is shown in Fig. 5. The rms of the residuals after subtracting the best fit power law (linear fit on the log scale of Fig. 5) gives the the magnitude errors listed with the magnitudes on column 4, Table 3. Columns 5 and 6 give the corresponding flux density and flux error, using the zero point flux densities for the J, H, and K bands of 1594, 1024, and 667 Jy from Cohen et al. (2003). In the J and H bands both errors can be smaller than 0.1 magnitudes.

¹ <https://irsa.ipac.caltech.edu/cgi-bin/Gator/nph-dd>

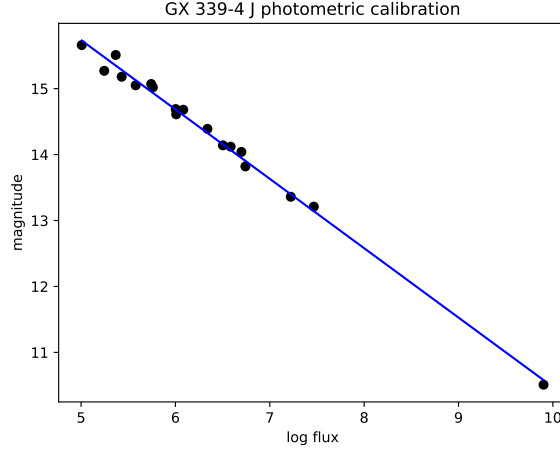


Figure 5. SMARTS photometry of GX 339-4 at J band. The reference stars are fitted with two dimensional Gaussians, whose integrals are assumed to be proportional to the stars' flux. The log of the flux is fitted to the catalog magnitudes of the stars from the 2MASS survey. The scatter around this relation gives the magnitude error in column 4 of Table 3.

Although XRBs are variable stars, both due to rapid changes in the optical and infrared luminosities of the X-ray emission region, and to variability in the companion star, a comparison between the magnitudes measured in this project with the 2MASS catalog values shows that there is generally not much change between the two epochs. We compare the observed J band magnitudes with the values in the 2MASS point source catalog and the few available V band magnitudes from the APASS catalog for all sources on figure 6. There has been surprisingly little variation between the 2MASS epoch and the date of these observations, roughly ten years later, except for GX339-4, which is much brighter than in the catalog (J=13.75 vs. 15.91 in the point source catalog, and H=12.99 vs. 15.40). A similar result is found by Shidatsu et al. (2011) who measure J=13.66 with a slow brightening to J=12.9 over a month of observations in March, 2009.

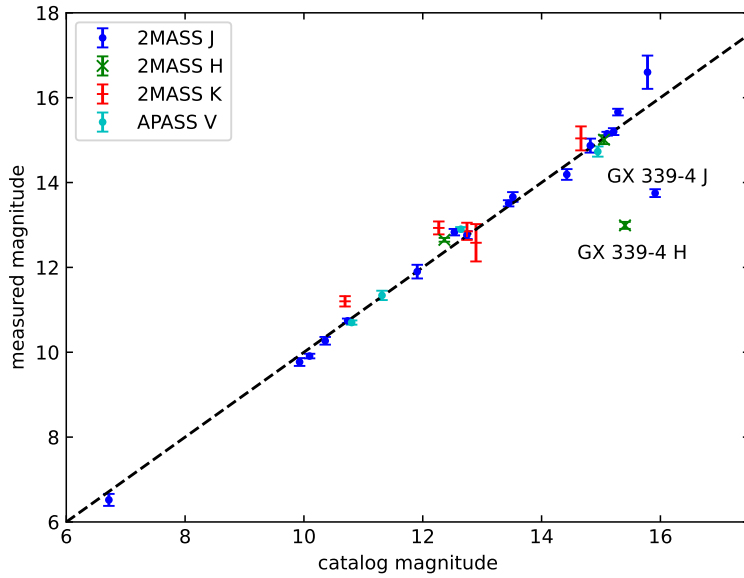


Figure 6. Comparison between the measured magnitudes of the X-ray sources vs. their catalog values. GX 339-4 shows very significant difference from the 2MASS result, at the level of 30σ . The other sources are all consistent within 3σ . Only sources with positions within $2''$ of the catalog values are included.

2.3. Optical Photometry

The optical V band data were also taken with the SMARTS 1.3m at CTIO, with the ANDICAM-CCD based on the Fairchild 447 detector. The images were flat fielded and bad pixels flagged before aligning, and median filtered for each night. Coordinates were determined using five or six reference stars visible on the 2MASS J or H band images in the KARMA task KOORDS. Comparison stars near the X-ray source were used for photometric calibration. Magnitudes at V band for these stars were taken from the APASS catalog (Henden et al. 2015). Stars were checked and rejected if there were nearby objects that could confuse the Gaussian fitting. Reference stars in the optical are illustrated on Fig. 7. The photometric calibration is done using these stars similarly to the 2MASS calibration for the IR observations described above. Fig. 8 illustrates the star flux vs. APASS catalog magnitudes for GX 339-4, similar to Fig. 5. The errors following the magnitudes in column 4 are the rms scatter of the reference stars about the best fit linear relation between their magnitudes and the integral of their fitted Gaussians on Fig. 8, or the formal error in the constant term of the fit to the reference star magnitudes, whichever is greater. Fluxes and flux errors are derived from the magnitudes and their errors assuming the Johnson V band zero magnitude flux density of 3780 Jy (Cox 2000).

Fig. Set 7. SMARTS V band images

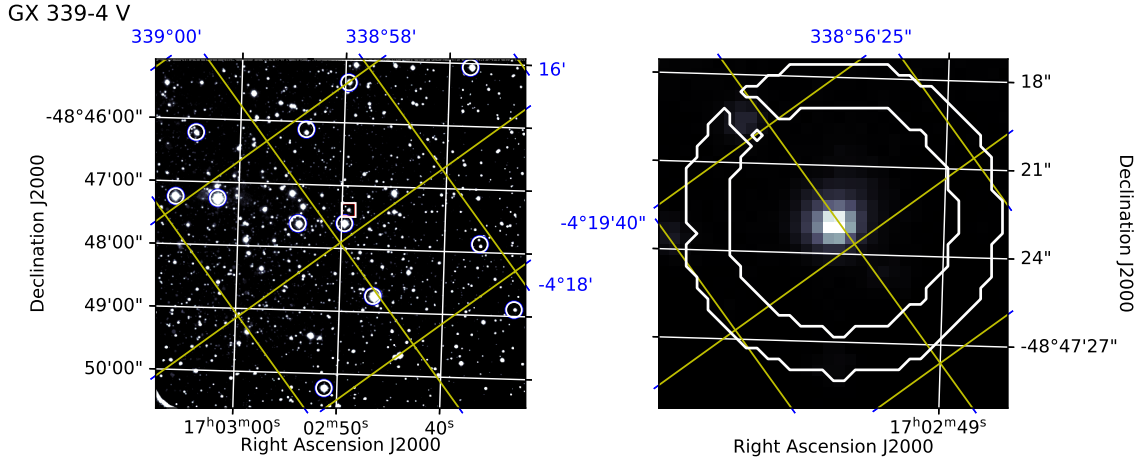


Figure 7. SMARTS image of the field of GX 339-4 at V band. Photometric reference stars are indicated by blue circles, the X-ray source by a red square, with side lengths 32 pixels = 11.9". The right panel shows an expanded image of the red square area, with the white contour indicating the area used to fit the background. The complete figure set (28 images) is available in the online journal.

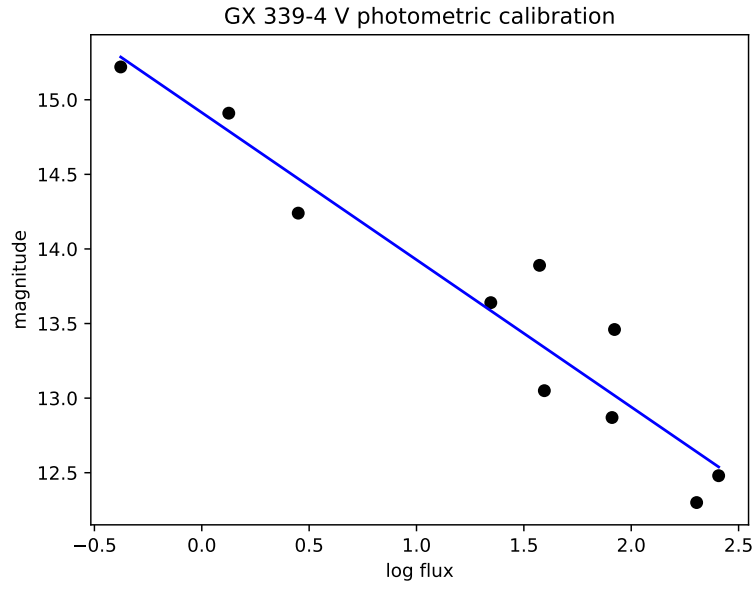


Figure 8. SMARTS photometry of GX 339-4 at V band, similar to figure 5, but using reference stars from the APASS catalog.

Table 3. Infra-Red and Optical Magnitudes

Source	Band	MJD	Magnitude	Flux Density mJy	Flux Error mJy
Black Holes					
XTE J1550-564	J ^a	54281	18.5±1.2	0.06	0.04
GRO J1655-40	K	54281-54286	12.85±0.2	4.8	0.8
GRO J1655-40	J	54281-54286	13.66±0.11	5.48	0.53
GRO J1655-40	V	all days	16.48±0.17	1.0	0.1
GX 339-4	H	54286-54286	12.99±0.08	6.52	0.46
GX 339-4	J	54281-54286	13.75±0.09	5.04	0.40
GX 339-4	V	all days	16.24±0.26	1.3	0.3
V4641 Sgr	K	54283-54286	12.93±0.14	25	3
V4641 Sgr	H	54283-54286	12.65±0.04	8.92	0.32
V4641 Sgr	J	54283-54286	12.83±0.07	11.76	0.84
V4641 Sgr	V	all days	14.88±0.14	4.2	0.4
GRS1915+105	K	54281-54286	12.6±0.4	6.2	2.1
Z Sources					
Cir X-1	K	54282+54286	11.20±0.12	22	2
Cir X-1	J	54282+54286	12.76±0.09	12.5	1.0
Cir X-1	V	54285	19.5±0.2	0.06	0.02
Sco X-1	J	54282	11.9±0.2	28	4.7
Sco X-1	V	54281	12.90±0.05	26	1
XTE J1701-462	K	54282-54284	15.04±0.30	0.64	0.16
XTE J1701-462	H	54282-54284	15.12±0.15	0.92	0.13
XTE J1701-462	J	54282-54284	16.8±0.2	0.30	0.07
XTE J1701-462	V	54282+54283	19±0.4	0.09	0.04
GX 349+2	J	54282+54286	15.20±0.07	1.33	0.09
GX 349+2	V	54285	17.37±0.16	0.43	0.03
GX 5-1 ^b	J	54282	9.77±0.09	197	16
GX 5-1 ^b	V	54280	11.34±0.20	110	11
GX 17+2	J	54282+54285	15.15±0.04	1.39	0.05
GX 17+2	V	54284	17.27±0.09	0.47	0.04
Atoll Sources					
4U 1254-690	J ^c	54282	16.9±0.4	0.28	0.10
4U 1254-690	V	54281	18.9±0.1	0.10	0.02
Cen X-4	K	54282-54286	15.0±0.2	0.67	0.11
Cen X-4	H	54282-54286	15.01±0.10	1.01	0.09
Cen X-4	V	54286	17.63±0.16	0.34	0.05
4U 1543-624 ^b	J	54283+54284	>17	<0.25	...
4U 1543-624 ^b	V	54282+54283	15.23±0.09	3.1	0.2

Table 3 continued on next page

Table 3 (*continued*)

Source	Band	MJD	Magnitude	Flux Density	Flux Error
				mJy	mJy
4U 1608-52 ^b	J	54286	> 17	< 0.25	...
4U 1608-52 ^b	V	54285	17.5±0.2	0.38	0.06
4U 1636-536 ^b	J ^d	54284	15.9±0.2	0.70	0.12
4U 1636-536	V	54283	18.2±0.09	0.2	0.03
MXB 1658-298	J	54284	>17	<0.25	...
MXB 1658-298	V	54283	>19	<0.09	...
GX 9+9 ^b	J	54284+54285	14.19±0.12	3.36	0.35
GX 9+9 ^b	V	54283+54284	15.31±0.18	2.8	0.4
4U 1735-444	J ^c	54285	16.52±0.14	0.39	0.06
4U 1735-444	V	54284	17.2±0.5	0.5	0.1
4U 1822-371	J	54285	15.66±0.06	0.87	0.05
4U 1822-371	V	54284	16.2±0.9	1.3	0.5
Aql X-1	J	54286	16.6±0.4	0.37	0.11
Aql X-1	V	54283+54285	19.4±0.4	0.07	0.02
Pulsars					
SMC X-3	J	54282	14.87±0.16	1.80	0.25
SMC X-3	V	54280+54281	14.73±0.19	4.8	0.5
SMC X-1	J	54281+54282	13.51±0.11	6.3	0.4
SMC X-1	V	54280+54281	13.16±0.08	20.6	2.0
Cen X-3	J	54283	10.74±0.05	80.6	3.6
Cen X-3	V	54282	13.32±0.08	17.8	0.8
GX 301-2	J	54283	6.52±0.10	3930	480
GX 301-2	V	54282	10.70±0.07	198	9
4U 1538-52	J	54283	10.27±0.09	124	10
4U 1538-52	V	54282	13.6±0.3	14	2
GX 1+4	J	54284	9.91±0.05	173	8
GX 1+4	V	54283	17.07±0.14	0.56	0.03
4U 1907+097	J	54281	12.66±0.10	13.8	1.2
4U 1907+097	V	54281	18.0±0.08	0.24	0.02

^aposition discrepant by 9''^bconfused by nearby bright star^cposition discrepant by 8''^dposition discrepant by 6''

2.4. UV Observations – Swift UVOT

Neil Gehrels Swift Observatory is a multi-wavelength observatory dedicated to the study of gamma-ray burst (GRB) science and transient sources. It has three instruments that observe simultaneously in the gamma-ray, X-ray, ultraviolet, and optical wavebands, which work in tandem to provide rapid identification and multi-wavelength follow-up of GRBs and transient sources. The three instruments are the (1) Burst Alert Telescope (BAT) observing at 15 - 150 keV, (2) X-ray Telescope (XRT) observing at 0.3 - 10 keV, and (3) UV/Optical Telescope (UVOT) observing at 170 - 600 nm. More details about the mission can be found in [Gehrels et al. \(2004\)](#).

We requested and acquired multiple pointed Swift observations for 15 sources during the week of our observing campaign. In addition, for all of the sources observed in our campaign, we made BAT lightcurves from the Swift/BAT hard X-ray transient monitor data.

The UltraViolet and Optical Telescope (UVOT) is a diffraction-limited 30 cm (12 inch aperture) Ritchey-Chrétien reflector, sensitive to magnitude 22.3 in a 17 minute exposure. The Ritchey-Chrétien telescope has a f/2.0 primary that is re-imaged to f/13 by the secondary. This results in pixels that are $0.502''$ over its $17'$ square FoV. The detector is an intensified CCD with seven broadband UVOT filters (white, U, V, B, UVW1, UVM2, and UVW2) covering the 170 - 600 nm wavelength range. For more details on UVOT see [Roming et al. \(2005\)](#).

For most of the Swift observations a UVOT observation in image mode was made in one or more of the filters. For these observations we analyzed the data using the standard UVOT analysis threads² using the tools for Swift data analysis found in the Heasoft software package³. For most datasets we used the pipeline-reduced summed image in the data products. For a few observations for which pipeline-reduced products were not complete it was necessary to sum the images using the tool *uvotimsum*. For each source we created a circular $5''$ radius extraction region centered on the source and a nearby background extraction region (with no obvious sources) with at least four times the area of the source. For each band observed we ran *uvotsource* using a background threshold of 3 sigma to obtain the fluxes and their errors. For the Swift/UVOT the PSF is 2.5 arcsec and the pixel scale is 0.502. This limits the resolution and sources that we include or exclude from the source detection region. Most of the Swift/UVOT observations are in one of the ultraviolet filters. In the ultraviolet most stars drop in flux and most of the XRBs have significant emission because of the accretion disk. This limits the number of sources that are detected. For the significant Swift/UVOT detections we find well defined sources at the positions of the XRBs. For fainter sources we exclude any confusing sources that overlap the source detection region. For detected sources we determine flux densities and errors given in table 4. For sources not detected we give upper limits. The conversion between UVOT band and frequency are given in table 5.

Table 4. SWIFT UVOT Results

Source	Obsid ^a	Band	Exposure (seconds)	Mag.	Error (stat.)	Error (sys.)	Flux (Jy)	Flux Error Jy (stat.)	Flux Error Jy (sys.)
Black Holes									
LMC X-3	00037080001	V	188.62	16.71	0.08	0.01	7.51×10^{-4}	5.5×10^{-5}	2.0×10^{-6}
LMC X-3	00037080001	B	188.63	16.79	0.04	0.02	7.77×10^{-4}	3.2×10^{-5}	3.0×10^{-6}
LMC X-3	00037080001	U	188.62	15.91	0.04	0.02	6.22×10^{-4}	2.3×10^{-5}	1.0×10^{-5}
LMC X-3	00037080001	UVW1	398.90	15.65	0.03	0.03	4.90×10^{-4}	1.5×10^{-5}	1.5×10^{-5}
LMC X-3	00037080001	UVM2	492.79	15.58	0.04	0.03	4.50×10^{-4}	1.5×10^{-5}	3.0×10^{-6}
LMC X-3	00037080001	UVW2	797.64	15.64	0.03	0.03	4.08×10^{-4}	1.0×10^{-5}	9.0×10^{-6}
LMC X-3	00037080002	V	176.45	16.82	0.08	0.01	6.80×10^{-4}	5.0×10^{-5}	2.0×10^{-6}
LMC X-3	00037080002	B	176.62	16.93	0.05	0.02	6.88×10^{-4}	3.1×10^{-5}	3.0×10^{-6}

Table 4 continued on next page

² <https://www.swift.ac.uk/analysis/uvot/>

³ <https://heasarc.gsfc.nasa.gov/docs/software/heasoft/>

Table 4 (continued)

Source	Obsid ^a	Band	Exposure	Mag.	Error	Error	Flux	Flux Error	Flux Error
			(seconds)		(stat.)	(sys.)	(Jy)	Jy (stat.)	Jy (sys.)
LMC X-3	00037080002	U	176.50	16.01	0.04	0.02	5.69×10^{-4}	2.2×10^{-5}	9.0×10^{-6}
LMC X-3	00037080002	UVW1	350.68	15.72	0.03	0.03	4.62×10^{-4}	1.5×10^{-5}	1.4×10^{-5}
LMC X-3	00037080002	UVM2	470.71	15.64	0.04	0.03	4.27×10^{-4}	1.5×10^{-5}	3.0×10^{-6}
LMC X-3	00037080002	UVW2	705.04	15.64	0.03	0.03	4.09×10^{-4}	1.1×10^{-5}	9.0×10^{-6}
LMC X-3	00037080003	V	191.20	16.70	0.07	0.01	7.63×10^{-4}	4.9×10^{-5}	3.0×10^{-6}
LMC X-3	00037080003	B	191.25	16.80	0.04	0.02	7.70×10^{-4}	3.0×10^{-5}	3.0×10^{-6}
LMC X-3	00037080003	U	191.28	15.93	0.04	0.02	6.12×10^{-4}	2.2×10^{-5}	9.0×10^{-6}
LMC X-3	00037080003	UVW1	383.15	15.67	0.03	0.03	4.81×10^{-4}	1.5×10^{-5}	1.5×10^{-5}
LMC X-3	00037080003	UVM2	518.15	15.61	0.04	0.03	4.37×10^{-4}	1.5×10^{-5}	3.0×10^{-6}
LMC X-3	00037080003	UVW2	769.09	15.70	0.03	0.03	3.85×10^{-4}	1.0×10^{-5}	8.0×10^{-6}
GX339-4	00030953004	B	7.12	17.42	0.25	0.02	4.35×10^{-4}	9.9×10^{-5}	2.0×10^{-6}
GX339-4	00030953004	U	83.39	17.66	0.13	0.02	1.25×10^{-4}	1.5×10^{-5}	2.0×10^{-6}
GX339-4	00030953004	UVW1	382.41	18.56	0.14	0.03	3.36×10^{-5}	4.3×10^{-6}	1.0×10^{-6}
GX339-4	00030953005	V	136.90	16.45	0.07	0.01	9.62×10^{-4}	6.2×10^{-5}	3.0×10^{-6}
GX339-4	00030953005	B	136.91	17.61	0.07	0.02	3.68×10^{-4}	2.4×10^{-5}	1.0×10^{-6}
GX339-4	00030953005	U	136.91	17.37	0.08	0.02	1.63×10^{-4}	1.3×10^{-5}	3.0×10^{-6}
GX339-4	00030953005	UVW1	274.701	18.41	0.14	0.03	3.86×10^{-5}	5.1×10^{-6}	1.2×10^{-6}
GX339-4	00030953005	UVM2	297.36	19.71	0.35	0.03	1.01×10^{-5}	3.3×10^{-6}	1.0×10^{-7}
GX339-4	00030953005	UVW2	550.28	19.99	0.29	0.03	7.44×10^{-6}	2.00×10^{-6}	1.6×10^{-7}
GX339-4	00030953006	V	52.94	16.54	0.11	0.01	8.83×10^{-4}	9.3×10^{-5}	3.0×10^{-6}
GX339-4	00030953006	B	52.93	17.50	0.11	0.02	4.04×10^{-4}	4.0×10^{-5}	2.0×10^{-6}
GX339-4	00030953006	U	52.93	17.31	0.13	0.02	1.72×10^{-4}	2.0×10^{-5}	3.0×10^{-6}
GX339-4	00030953006	UVW1	105.08	18.50	0.25	0.03	3.55×10^{-5}	8.3×10^{-6}	1.1×10^{-6}
GX339-4	00030953006	UVM2	135.91	19.36	0.36	0.03	1.39×10^{-5}	4.6×10^{-6}	1.0×10^{-7}
GX339-4	00030953006	UVW2	211.39	19.16	0.24	0.03	1.60×10^{-5}	3.5×10^{-6}	3.0×10^{-7}
1E1740-29	00030960001	U	3785.47	21.19	*	*	4.81×10^{-6}	*	*
GRS1758-258	00030961001	U	3257.18	21.03	*	*	5.56×10^{-6}	*	*
4U 1957+11	00030960001	UVM2	3843.32	18.01	0.04	0.03	4.81×10^{-5}	2.0×10^{-6}	3.0×10^{-7}
Z Sources									
Cir X-1	00030268024	UVM2	1024.19	16.02	*	*	2.99×10^{-4}	*	*
Cir X-1	00030268025	UVW2	1208.71	20.68	*	*	3.93×10^{-6}	*	*
GX17+2	00035340006	UVW2	3353.89	21.28	*	*	2.27×10^{-6}	*	*
GX349+2	00036690002	UVM2	4533.23	21.27	*	*	2.38×10^{-6}	*	*
Atoll Sources									
4U 1608-52	00030791018	UVW1	1240.11	20.83	*	*	4.15×10^{-6}	*	*
4U 1608-52	00030791019	U	1005.07	20.57	0.29	0.02	8.52×10^{-6}	2.25×10^{-6}	1.3×10^{-7}
4U 1608-52	00030791020	UVM2	902.65	20.55	*	*	4.63×10^{-6}	*	*
4U 1608-52	00030791021	U	1119.99	20.32	0.33	0.02	1.08×10^{-5}	2.20×10^{-6}	2.0×10^{-7}
4U 1608-52	00030791022	UVM2	1475.56	20.92	*	*	3.29×10^{-6}	*	*
4U 1608-52	00030791023	U	945.80	20.41	0.26	0.02	9.93×10^{-6}	2.39×10^{-6}	1.5×10^{-7}

Table 4 continued on next page

Table 4 (*continued*)

Source	Obsid ^a	Band	Exposure	Mag.	Error	Error	Flux	Flux Error	Flux Error
			(seconds)		(stat.)	(sys.)	(Jy)	Jy (stat.)	Jy (sys.)
GX9+9	00030965001	UVW2	4086.32	16.32	0.02	0.03	2.18×10^{-4}	5.0×10^{-6}	5.0×10^{-6}
GX9+9	00030965003	UVM2	195.28	16.21	0.07	0.03	2.52×10^{-4}	1.5×10^{-5}	2.0×10^{-6}
GX354+0	00030964001	UVM2	3770.68	21.11	*	*	2.77×10^{-6}	*	*
4U 1735-44	00035338003	UVM2	3728.44	17.22	0.03	0.03	9.92×10^{-5}	3.1×10^{-6}	6.0×10^{-7}
Swift 1756-2508	00030952011	U	517.43	19.88	*	*	1.61×10^{-5}	*	*
Swift 1756-2508	00030952011	UVW1	6231.58	21.14	*	*	3.13×10^{-6}	*	*
Swift 1756-2508	00030952012	U	6390.68	21.25	*	*	4.57×10^{-6}	*	*
Swift 1756-2508	00030952013	UVM2	438.47	19.59	*	*	1.12×10^{-5}	*	*
Swift 1756-2508	00030952013	UVW2	6048.35	21.21	*	*	2.42×10^{-6}	*	*
4U 1822-37	00036691001	U	1660.69	14.40	0.02	0.02	2.50×10^{-3}	5.0×10^{-5}	4.0×10^{-5}
Pulsars									
SMC X-1	00035216002	UVW1	1569.52	11.11	0.03	0.03	3.20×10^{-2}	9.0×10^{-4}	1.0×10^{-3}

^aFor corresponding MJD start times see Table 6.

*the magnitude of the flux is an upper limit.

Swift/UVOT Filter	Freq. (Hz)
V	5.550×10^{14}
B	6.925×10^{14}
U	8.563×10^{14}
UVW1	1.138×10^{15}
UVM2	1.344×10^{15}
UVW2	1.477×10^{15}

Table 5. Swift/UVOT to Frequency conversion

2.5. X-ray Observations

2.5.1. Swift XRT

The XRT is a focusing X-ray telescope with a 110 cm^2 effective area, $23.6' \times 23.6'$ FOV, $18''$ resolution (half-power diameter), and $0.2 - 10 \text{ keV}$ energy range. The XRT uses a grazing incidence Wolter 1 telescope to focus X-rays onto a CCD detector. Further information on the XRT is given by [Burrows et al. \(2005\)](#).

The Swift observations were done in window timing mode (WT) for bright sources or photon counting mode (PC) for fainter sources. For bright sources the WT data consists of a 1-dimensional line. The spectral data extraction region used is a 40 pixel width box with a height large enough to include all of the photons centered on the source. One or more boxes are created at either end of the line to collect the background spectra. For fainter sources done in PC mode a circle with a 20 pixel radius was used along with a circular background having at least four times the source extraction area, at a position away from any sources on the detector. The Heasoft tool *xselect* is then used to extract the spectrum and filter the data.

The results of modelling the Swift/XRT spectra are shown on Table 6. All of the data sets were fitted with both disk black-body (DBB) and power-law (PL) models, as indicated in column 5. Comparing the χ^2 per degree of freedom (column 10) gives a good measure of the relative quality of the fits using the two models. In some cases they are nearly the same, e.g. Aql X-1 after MJD 54286. Column 8 gives the derived value of the hydrogen column density

along the path to the source. For comparison, column 9 gives the total column density of Milky Way HI from the HEASARC Tools⁴ using data from the HI4PI survey (HI4PI Collaboration et al. 2016). The quality of the fits (statistics and residuals) were such that fitting with more complicated models was not warranted. The corresponding best fit temperature is in column 7 and the power-law index in column 6. The quality of the fit is indicated by chi-square and the corresponding number of degrees of freedom is the denominator in column 10. The derived flux in the 0.5 to 10 keV band is given in column 10. The Z source Cir X-1 and the pulsar 4U1822-37 have such shallow slopes ($\Gamma = 0.56$ for the PL), that it is difficult to fit the temperature in a DBB model.

The issue of pile-up is examined for each spectrum. If the PC mode is less than ~ 0.5 cts s⁻¹ or the WT mode is less than 100 cts s⁻¹ then pile-up is not a significant issue. If pile-up is a possible problem we use standard procedures⁵ to determine the impact and how to mitigate it. The main approach to correct pile-up is to eliminate inner pixels of the extraction region and re-extract the spectrum and use only grade 0 events.

XRT data were taken during our campaign week ($54280 \leq \text{MJD} \leq 54287$) for 13 sources on Table 6. Data for three other sources were taken a few days before or after our campaign, and they are included on the Table and on the spectral energy distributions plotted in Sec. 3 below. These are LMC X-3, observed some 12 to 15 days after the end of the campaign, 4U 1822-37, observed four days before the start, and SMC X-1, observed nine days before the start. For LMC X-3, this time offset spans a period of rapid variation in the source properties, as discussed in Sec. 3.

⁴ <https://heasarc.gsfc.nasa.gov/cgi-bin/Tools/w3nh/w3nh.pl>

⁵ <https://www.swift.ac.uk/analysis/xrt/pileup.php>

Table 6. Swift XRT Results

Source	Obsid	Start	Exposure	Model	Gamma	T	N _H	N _H (Gal.)	χ ²	F _x (0.5 – 10 keV)
		MJD	sec			keV	10 ²² cm ⁻²	10 ²² cm ⁻²	per d.o.f.	ergs cm ⁻² s ⁻¹
Black Holes										
1E1740-29	00030960001	54284.414	3803	PL	1.86 ^{+0.31} _{-0.28}	*	9.62 ^{+1.57} _{-1.32}	1.50	68.83/75	1.14 ^{+0.02} _{-0.12} × 10 ⁻¹⁰
1E1740-29	00030960001	54284.414	3803	DBB	*	2.77 ^{+0.57} _{-0.41}	7.83 ^{+1.07} _{-0.90}	1.50	64.93/75	1.11 ^{+0.01} _{-0.29} × 10 ⁻¹⁰
GRS1758-258	00030961001	54284.547	1951	PL	2.65 ^{+0.05} _{-0.05}	*	1.59 ^{+0.05} _{-0.05}	0.60	538.88/504	1.37 ^{+0.01} _{-0.02} × 10 ⁻⁹
GRS1758-258	00030961001	54284.547	1951	DBB	*	1.17 ^{+0.03} _{-0.03}	0.95 ^{+0.03} _{-0.03}	0.60	900.42/504	1.22 ^{+0.01} _{-0.01} × 10 ⁻⁹
4U1957+115	00030959001	54282.547	1744	DBB	*	1.43 ^{+0.01} _{-0.01}	0.08 ^{+0.01} _{-0.01}	0.12	731.42/626	7.84 ^{+0.04} _{-0.04} × 10 ⁻¹⁰
4U1957+115	00030959001	54282.547	1744	PL	1.96 ^{+0.09} _{-0.09}	*	0.27 ^{+0.004} _{-0.004}	0.12	2495.85/626	8.41 ^{+0.03} _{-0.04} × 10 ⁻¹⁰
GX339-4	00030953004	54281.785	493.4	PL	1.62 ^{+0.13} _{-0.12}	*	0.42 ^{+0.07} _{-0.06}	0.39	84.54/91	1.78 ^{+0.07} _{-0.07} × 10 ⁻¹⁰
GX339-4	00030953004	54281.785	493.4	DBB	*	1.86 ^{+0.21} _{-0.18}	0.23 ^{+0.04} _{-0.04}	0.39	96.29/91	1.56 ^{+0.01} _{-0.17} × 10 ⁻¹⁰
GX339-4	00030953005	54285.195	1659	PL	1.56 ^{+0.06} _{-0.05}	*	0.38 ^{+0.03} _{-0.03}	0.39	307.36/315	2.47 ^{+0.04} _{-0.05} × 10 ⁻¹⁰
GX339-4	00030953005	54285.195	1659	DBB	*	2.04 ^{+0.11} _{-0.10}	0.21 ^{+0.02} _{-0.02}	0.39	334.20/315	2.23 ^{+0.13} _{-0.04} × 10 ⁻¹⁰
GX339-4	00030953006	54288.14	1149	PL	1.63 ^{+0.06} _{-0.06}	*	0.39 ^{+0.03} _{-0.03}	0.39	225.10/267	2.60 ^{+0.06} _{-0.05} × 10 ⁻¹⁰
GX339-4	00030953006	54288.14	1149	DBB	*	1.90 ^{+0.11} _{-0.10}	0.21 ^{+0.02} _{-0.02}	0.39	264.41/267	2.33 ^{+0.04} _{-0.07} × 10 ⁻¹⁰
LMC X-3	00037080001	54299.574	2405	DBB	*	1.18 ^{+0.03} _{-0.03}	0.03 ^{+0.01} _{-0.01}	0.04	367.23/321	5.36 ^{+0.05} _{-0.07} × 10 ⁻¹⁰
LMC X-3	00037080001	54299.574	2405	PL	2.16 ^{+0.04} _{-0.04}	*	0.21 ^{+0.01} _{-0.01}	0.04	542.66/321	5.81 ^{+0.07} _{-0.09} × 10 ⁻¹⁰
LMC X-3	00037080002	54300.773	2133	DBB	*	1.17 ^{+0.03} _{-0.03}	0.03 ^{+0.01} _{-0.01}	0.04	351.46/303	5.58 ^{+0.04} _{-0.07} × 10 ⁻¹⁰
LMC X-3	00037080002	54300.773	2133	PL	2.10 ^{+0.05} _{-0.05}	*	0.19 ^{+0.02} _{-0.01}	0.04	510.27/303	6.18 ^{+0.10} _{-0.07} × 10 ⁻¹⁰
LMC X-3	00037080003	54302.254	2303	DBB	*	1.16 ^{+0.03} _{-0.03}	0.03 ^{+0.01} _{-0.01}	0.04	307.34/336	5.61 ^{+0.10} _{-0.05} × 10 ⁻¹⁰
LMC X-3	00037080003	54302.254	2303	PL	2.09 ^{+0.04} _{-0.04}	*	0.18 ^{+0.01} _{-0.01}	0.04	573.16/336	6.22 ^{+0.11} _{-0.08} × 10 ⁻¹⁰
Atoll Sources										
Aql X-1	00030796021	54279.777	1935	PL	1.83 ^{+0.09} _{-0.09}	*	0.45 ^{+0.05} _{-0.05}	0.31	167.75/170	2.47 ^{+0.06} _{-0.07} × 10 ⁻¹⁰
Aql X-1	00030796021	54279.777	1935	DBB	*	1.55 ^{+0.11} _{-0.10}	0.21 ^{+0.03} _{-0.03}	0.31	201.30/170	2.12 ^{+0.05} _{-0.08} × 10 ⁻¹⁰
Aql X-1	00030796022	54283.473	2228	PL	2.55 ^{+0.22} _{-0.20}	*	0.63 ^{+0.10} _{-0.09}	0.31	57.53/57	1.78 ^{+0.08} _{-0.10} × 10 ⁻¹¹
Aql X-1	00030796022	54283.473	2228	DBB	*	1.00 ^{+0.11} _{-0.10}	0.28 ^{+0.07} _{-0.06}	0.31	89.00/57	1.53 ^{+0.03} _{-0.13} × 10 ⁻¹⁰
Aql X-1	00030796023	54286.133	2462	PL	4.67 ^{+1.32} _{-1.08}	*	0.96 ^{+0.42} _{-0.33}	0.31	191.11/971 [†]	6.72 ^{+0.56} _{-1.84} × 10 ⁻¹³
Aql X-1	00030796023	54286.133	2462	DBB	*	0.48 ^{+0.16} _{-0.11}	0.38 ^{+0.26} _{-0.19}	0.31	193.05/971 [†]	6.73 ^{+0.01} _{-0.40} × 10 ⁻¹³
Aql X-1	00030796024	54287.492	0	PL	*	*	*	0.31	*	*

Table 6 continued on next page

Table 6 (continued)

Source	Obsid	Start	Exposure	Model	Gamma	T	N _H	N _H (Gal.)	χ^2	F _x (0.5 – 10 keV)
		MJD	sec			keV	10 ²² cm ⁻²	10 ²² cm ⁻²	per d.o.f.	ergs cm ⁻² s ⁻¹
Aql X-1	00030796024	54287.492	0	DBB	*	*	*	0.31	*	*
Aql X-1	00030796025	54288.55	2168	PL	3.74 ^{+0.96} _{-0.82}	*	0.72 ^{+0.30} _{-0.25}	0.31	213.13/971 [†]	9.63 ^{+0.47} _{-2.46} × 10 ⁻¹³
Aql X-1	00030796025	54288.55	2168	DBB	*	0.65 ^{+0.20} _{-0.14}	0.26 ^{+0.18} _{-0.14}	0.31	218.49/971 [†]	9.63 ^{+0.55} _{-4.33} × 10 ⁻¹³
Aql X-1	00030796026	54289.773	3376	PL	3.07 ^{+0.66} _{-0.58}	*	0.43 ^{+0.19} _{-0.16}	0.31	266.89/971 [†]	9.77 ^{+0.73} _{-1.59} × 10 ⁻¹³
Aql X-1	00030796026	54289.773	3376	DBB	*	0.85 ^{+0.24} _{-0.16}	0.09 ^{+0.10} _{-0.08}	0.31	279.59/971 [†]	9.71 ^{+0.57} _{-2.31} × 10 ⁻¹³
4U1608-52	00030791018	54279.91	1262	DBB	*	1.83 ^{+0.03} _{-0.03}	0.86 ^{+0.02} _{-0.02}	1.66	878.54/706	3.70 ^{+0.02} _{-0.02} × 10 ⁻⁹
4U1608-52	00030791018	54279.91	1262	PL	1.93 ^{+0.03} _{-0.03}	*	1.36 ^{+0.03} _{-0.03}	1.66	1233.45/706	4.03 ^{+0.03} _{-0.01} × 10 ⁻⁹
4U1608-52	00030791019	54280.926	1006	DBB	*	1.89 ^{+0.05} _{-0.05}	0.83 ^{+0.03} _{-0.03}	1.66	683.90/597	1.91 ^{+0.02} _{-0.02} × 10 ⁻⁹
4U1608-52	00030791019	54280.926	1006	PL	1.87 ^{+0.04} _{-0.04}	*	1.31 ^{+0.05} _{-0.04}	1.66	719.83/597	2.10 ^{+0.01} _{-0.02} × 10 ⁻⁹
4U1608-52	00030791020	54282.05	905.7	DBB	*	1.62 ^{+0.03} _{-0.03}	0.82 ^{+0.02} _{-0.02}	1.66	707.25/607	2.46 ^{+0.02} _{-0.02} × 10 ⁻⁹
4U1608-52	00030791020	54282.05	905.7	PL	2.08 ^{+0.04} _{-0.03}	*	1.33 ^{+0.04} _{-0.04}	1.66	758.20/607	2.71 ^{+0.02} _{-0.02} × 10 ⁻⁹
4U1608-52	00030791021	54284.863	1177	PL	2.27 ^{+0.06} _{-0.05}	*	1.24 ^{+0.05} _{-0.05}	1.66	437.94/462	8.26 ^{+0.09} _{-0.11} × 10 ⁻¹⁰
4U1608-52	00030791021	54284.863	1177	DBB	*	1.39 ^{+0.04} _{-0.04}	0.73 ^{+0.03} _{-0.03}	1.66	571.69/462	7.32 ^{+0.06} _{-0.11} × 10 ⁻¹⁰
4U1608-52	00030791022	54286.336	1483	PL	1.90 ^{+0.03} _{-0.03}	*	0.89 ^{+0.02} _{-0.02}	1.66	690.01/617	1.48 ^{+0.01} _{-0.01} × 10 ⁻⁹
4U1608-52	00030791022	54286.336	1483	DBB	*	1.75 ^{+0.02} _{-0.04}	0.52 ^{+0.02} _{-0.01}	1.66	1134.30/617	1.34 ^{+0.01} _{-0.01} × 10 ⁻⁹
4U1608-52	00030791023	54288.004	950	DBB	*	2.15 ^{+0.10} _{-0.09}	0.69 ^{+0.04} _{-0.04}	1.66	386.75/433	8.09 ^{+0.06} _{-0.19} × 10 ⁻¹⁰
4U1608-52	00030791023	54288.004	950	PL	1.66 ^{+0.06} _{-0.06}	*	1.06 ^{+0.06} _{-0.06}	1.66	410.99/433	8.82 ^{+0.13} _{-0.14} × 10 ⁻¹⁰
4U1735-44	00035338003	54282.32	1818	PL	1.62 ^{+0.02} _{-0.02}	*	0.30 ^{+0.01} _{-0.01}	0.28	779.33/652	3.66 ^{+0.02} _{-0.01} × 10 ⁻⁹
4U1735-44	00035338003	54282.32	1818	DBB	*	1.87 ^{+0.03} _{-0.03}	0.14 ^{+0.01} _{-0.01}	0.28	936.38/652	3.27 ^{+0.02} _{-0.03} × 10 ⁻⁹
GX354+0	00030964001	54286.4	3505	PL	1.82 ^{+0.04} _{-0.04}	*	2.88 ^{+0.07} _{-0.07}	1.30	816.74/727	1.25 ^{+0.01} _{-0.01} × 10 ⁻⁹
GX354+0	00030964001	54286.4	3505	DBB	*	2.36 ^{+0.06} _{-0.05}	2.04 ^{+0.04} _{-0.04}	1.30	793.41/727	1.19 ^{+0.01} _{-0.01} × 10 ⁻⁹
GX9+9	00030965001	54285.74	4154	DBB	*	1.84 ^{+0.02} _{-0.02}	0.17 ^{+0.01} _{-0.01}	0.19	936.83/781	3.90 ^{+0.01} _{-0.01} × 10 ⁻⁹
GX9+9	00030965001	54285.74	4154	PL	1.68 ^{+0.01} _{-0.01}	*	0.36 ^{+0.01} _{-0.01}	0.19	2645.35/781	4.26 ^{+0.01} _{-0.01} × 10 ⁻⁹
GX9+9	00030965002	54285.137	1205	DBB	*	1.97 ^{+0.03} _{-0.03}	0.17 ^{+0.01} _{-0.01}	0.19	748.38/705	4.68 ^{+0.03} _{-0.03} × 10 ⁻⁹
GX9+9	00030965002	54285.137	1205	PL	1.58 ^{+0.02} _{-0.02}	*	0.34 ^{+0.01} _{-0.01}	0.19	1333.34/705	5.16 ^{+0.03} _{-0.02} × 10 ⁻⁹
GX9+9	00030965003	54286.613	186.9	DBB	*	1.96 ^{+0.08} _{-0.07}	0.18 ^{+0.01} _{-0.01}	0.19	427.19/403	4.26 ^{+0.05} _{-0.07} × 10 ⁻⁹
GX9+9	00030965003	54286.613	186.9	PL	1.58 ^{+0.04} _{-0.04}	*	0.35 ^{+0.02} _{-0.02}	0.19	530.08/403	4.69 ^{+0.06} _{-0.06} × 10 ⁻⁹
Z Sources										
Cir X-1	00030268024	54278.906	1016	PL	0.85 ^{+0.38} _{-0.35}	*	2.09 ^{+0.73} _{-0.59}	1.63	25.51/27	4.98 ^{+0.15} _{-0.88} × 10 ⁻¹¹

Table 6 continued on next page

Table 6 (*continued*)

Source	Obsid	Start	Exposure	Model	Gamma	T	N _H	N _H (Gal.)	χ^2	F _x (0.5 – 10 keV)
		MJD	sec			keV	10 ²² cm ⁻²	10 ²² cm ⁻²	per d.o.f.	ergs cm ⁻² s ⁻¹
Cir X-1	00030268024	54278.906	1016	DBB	*	14.3 ^{††}	1.88 ^{+0.39} _{-0.31}	1.63	26.07/27	5.08 ^{+0.28} _{-0.30} × 10 ⁻¹¹
Cir X-1	00030268025	54285.062	1194	PL	0.79 ^{+0.69} _{-0.55}	*	0.62 ^{+0.76} _{-0.55}	1.63	3.69/9	1.22 ^{+0.11} _{-0.35} × 10 ⁻¹¹
Cir X-1	00030268025	54285.062	1194	DBB	*	12.79 ^{††}	0.55 ^{+0.50} _{-0.23}	1.63	3.69/9	1.23 ^{+0.12} _{-0.09} × 10 ⁻¹¹
GX17+2	00035340006	54285.605	3397	DBB	*	2.29 ^{+0.03} _{-0.03}	2.16 ^{+0.03} _{-0.03}	0.85	943.01/845	5.08 ^{+0.02} _{-0.02} × 10 ⁻⁹
GX17+2	00035340006	54285.605	3397	PL	1.85 ^{+0.01} _{-0.01}	*	3.02 ^{+0.03} _{-0.03}	0.85	1820.66/845	5.35 ^{+0.02} _{-0.02} × 10 ⁻⁹
GX17+2	00035340007	54285.89	284.5	DBB	*	2.00 ^{+0.09} _{-0.08}	2.20 ^{+0.10} _{-0.09}	0.85	401.96/465	3.70 ^{+0.02} _{-0.08} × 10 ⁻⁹
GX17+2	00035340007	54285.89	284.5	PL	2.04 ^{+0.08} _{-0.08}	*	3.18 ^{+0.16} _{-0.15}	0.85	464.77/465	3.95 ^{+0.04} _{-0.07} × 10 ⁻⁹
GX349+2	00036690002	54286.406	4604	DBB	*	2.39 ^{+0.02} _{-0.02}	0.70 ^{+0.01} _{-0.01}	0.47	934.99/868	8.42 ^{+0.02} _{-0.03} × 10 ⁻⁹
GX349+2	00036690002	54286.406	4604	PL	1.57 ^{+0.01} _{-0.01}	*	1.02 ^{+0.01} _{-0.01}	0.47	3201.71/868	8.96 ^{+0.02} _{-0.03} × 10 ⁻⁹
XTEJ1701-462	00030383022	54283.254	3991	PL	1.78 ^{+0.05} _{-0.05}	*	2.10 ^{+0.07} _{-0.07}	0.69	568.95/580	9.59 ^{+0.07} _{-0.11} × 10 ⁻⁹
XTEJ1701-462	00030383022	54283.254	3991	DBB	*	2.29 ^{+0.08} _{-0.08}	2.10 ^{+0.07} _{-0.07}	0.69	670.24/580	8.99 ^{+0.06} _{-0.17} × 10 ⁻⁹
Pulsars										
4U1822-37	00036691001	54276.16	1689	PL	0.56 ^{+0.03} _{-0.03}	*	0.01 ^{+0.01} _{-0.01}	0.10	584.55/445	4.87 ^{+0.08} _{-0.06} × 10 ⁻¹⁰
4U1822-37	00036691001	54276.16	1689	DBB	*	50.98 ^{††}	0.04 ^{+0.01} _{-0.01}	0.10	612.59/445	4.58 ^{+0.06} _{-0.04} × 10 ⁻¹⁰
SMC X-1	00035216002	54271.78	1583	PL	0.94 ^{+0.07} _{-0.07}	*	0.10 ^{+0.03} _{-0.03}	0.46	258.03/188	7.20 ^{+0.12} _{-0.20} × 10 ⁻¹⁰
SMC X-1	00035216002	54271.78	1583	DBB	*	5.13 ^{+1.34} _{-0.85}	0.05 ^{+0.02} _{-0.02}	0.46	268.09/188	6.97 ^{+0.01} _{-1.03} × 10 ⁻¹⁰

^a * denotes no value for this parameter. PL = power-law and DBB = disk black body. † indicates that, because of a low count rate, cstat was used for fitting instead of chi-squared, and the cstat result is given in place of χ^2 . †† This parameter is unconstrained by the fit for this model.

Table 7. SWIFT XRT Unabsorbed Fluxes

Source	Obsid	MJD Start	F_x (0.5 – 10 keV) $\times 10^{-10}$ ergs cm $^{-2}$ s $^{-1}$	F_x (2 – 10 keV) $\times 10^{-10}$ ergs cm $^{-2}$ s $^{-1}$
Black Holes				
LMC X-3	00037080001	54299.574	$5.51^{+0.12}_{-0.15}$	$3.21^{+0.11}_{-0.11}$
LMC X-3	00037080002	54300.773	$5.75^{+0.14}_{-0.14}$	$3.34^{+0.13}_{-0.13}$
LMC X-3	00037080003	54302.254	$5.77^{+0.12}_{-0.12}$	$3.33^{+0.11}_{-0.11}$
GX 339-4	00030953004	54281.785	$2.27^{+0.13}_{-0.15}$	$1.53^{+0.12}_{-0.12}$
GX 339-4	00030953005	54285.195	$3.06^{+0.08}_{-0.08}$	$2.12^{+0.07}_{-0.07}$
GX 339-4	00030953006	54288.14	$3.29^{+0.10}_{-0.09}$	$2.20^{+0.09}_{-0.09}$
1E 1740-29	00030960001	54284.414	$3.56^{+1.33}_{-0.75}$	$2.10^{+0.27}_{-0.20}$
GRS 1758-258	00030961001	54284.547	$45.3^{+2.4}_{-2.2}$	$13.9^{+0.2}_{-0.2}$
4U 1957+11	00030959001	54282.547	$8.39^{+0.07}_{-0.07}$	$5.51^{+0.06}_{-0.06}$
Z Sources				
Cir X-1	00030268024	54278.906	$0.63^{+0.06}_{-0.06}$	$0.55^{+0.05}_{-0.06}$
Cir X-1	00030268025	54285.062	$0.136^{+0.005}_{-0.03}$	$0.12^{+0.04}_{-0.03}$
XTE J1701-462	00030383022	54283.254	$175.^{+5.}_{-5.}$	$108^{+2.}_{-1.}$
GX 349+2	00036690002	54286.406	$103.^{+5.}_{-5.}$	$80.9^{+0.4}_{-0.4}$
GX 17+2	00035340006	54285.605	$74.3^{+0.5}_{-0.5}$	$58.1^{+0.4}_{-0.4}$
GX 17+2	00035340007	54285.89	$56.8^{+1.3}_{-0.9}$	$42.8^{+1.0}_{-1.0}$
Atoll Sources				
4U 1608-52	00030791018	54279.91	$48.9^{+0.4}_{-0.5}$	$35.7^{+0.4}_{-0.4}$
4U 1608-52	00030791019	54280.926	$24.9^{+0.3}_{-0.3}$	$18.4^{+0.3}_{-0.3}$
4U 1608-52	00030791020	54282.05	$33.3^{+0.4}_{-0.4}$	$23.2^{+0.3}_{-0.3}$
4U 1608-52	00030791021	54284.863	$18.0^{+0.8}_{-0.7}$	$7.91^{+0.17}_{-0.17}$
4U 1608-52	00030791022	54286.336	$23.8^{+0.4}_{-0.4}$	$13.7^{+0.2}_{-0.2}$
4U 1608-52	00030791023	54288.004	$9.98^{+0.22}_{-0.21}$	$7.67^{+0.21}_{-0.21}$
GX 354+0	00030964001	54286.4	$25.5^{+0.7}_{-0.6}$	$15.4^{+0.2}_{-0.2}$
GX 9+9	00030965001	54285.74	$42.7^{+0.2}_{-0.2}$	$31.3^{+0.2}_{-0.2}$
GX 9+9	00030965002	54285.137	$51.0^{+0.5}_{-0.5}$	$38.2^{+0.5}_{-0.5}$
GX 9+9	00030965003	54286.613	$46.5^{+1.1}_{-1.1}$	$34.8^{+1.1}_{-1.1}$
4U 1735-44	00035338003	54282.32	$44.6^{+0.4}_{-0.4}$	$30.0^{+0.4}_{-0.4}$
Aql X-1	00030796021	54279.777	$3.38^{+0.15}_{-0.14}$	$2.03^{+0.11}_{-0.11}$
Aql X-1	00030796022	54283.473	$0.382^{+0.062}_{-0.046}$	$0.129^{+0.015}_{-0.014}$
Aql X-1	00030796023	54286.133	$0.102^{+0.022}_{-0.019}$	$0.0025^{+0.002}_{-0.001}$
Aql X-1	00030796025	54288.55	$0.052^{+0.089}_{-0.027}$	$0.0044^{+0.0025}_{-0.0016}$
Aql X-1	00030796026	54289.773	$0.024^{+0.018}_{-0.008}$	$0.0047^{+0.0022}_{-0.0015}$
Pulsars				
SMC X-1	00035216002	54271.78	$7.45^{+0.31}_{-0.30}$	$6.36^{+0.33}_{-0.33}$
4U 1822-371	00036691001	54276.16	$4.87^{+0.12}_{-0.12}$	$4.46^{+0.12}_{-0.12}$

The energy range of the XRT is sufficiently broad to allow estimation of the intervening hydrogen column density, N_H , given in column 8 of Table 6. Based on N_H , the measured flux density can be corrected for absorption giving an estimate for the unabsorbed flux over two bands, (0.5 - 10 keV) and (2 - 10 keV). These are given for selected sources on Table 7.

2.5.2. RXTE ASM

Table 8. RXTE-ASM Results

Source	ASM Counts sec ⁻¹	Flux density mJy at 5 keV	Flux 2-10 keV ergs cm ⁻² s ⁻¹
Black Holes			
LMC X-3	<0.01		
LMC X-1	1.78	0.026	$7 \cdot 10^{-12}$
XTE J1550-564	<0.01		
4U1630-47	<0.01		
GROJ1655-40	1.9	<0.03	$<5.52 \cdot 10^{-10}$
GX339-4	<0.01		
1E 1740-29	<0.01		
GRS 1758-258	2.73	0.04	$7.76 \cdot 10^{-10}$
V4641 SGR	<0.01		
GRS1915+105	89.3	1.30	$2.54 \cdot 10^{-8}$
4U1957+115	2.09	0.03	$5.94 \cdot 10^{-10}$
Z Sources			
LMC X-2	1.90	0.28	$5.41 \cdot 10^{-10}$
Cir X-1	<0.01		
Sco X-1	906.51	13.15	$2.57 \cdot 10^{-7}$
GX340+0	28.94	0.42	$8.23 \cdot 10^{-9}$
XTE J1701-462	10.42	0.15	$2.96 \cdot 10^{-9}$
GX349+2	46.23	0.67	$0.31 \cdot 10^{-8}$
GX 5-1	66.61	0.97	$1.89 \cdot 10^{-8}$
GX 17+2	41.67	0.60	$0.18 \cdot 10^{-8}$
Atoll Sources			
EXO 0748-67	0.72	0.01	$2.04 \cdot 10^{-10}$
2S 0921-630	<0.01		
4U1254-69	2.30	0.03	$6.53 \cdot 10^{-10}$
Cen X-4	<0.01		
4U1543-624	2.04	0.03	$5.80 \cdot 10^{-10}$
4U1556-60	1.17	0.17	$3.32 \cdot 10^{-10}$
4U1608-522	12.90	0.19	$3.66 \cdot 10^{-9}$
4U1636-53	4.92	0.71	$1.40 \cdot 10^{-9}$
4U1658-298	2.02	0.03	$5.74 \cdot 10^{-10}$
4U1702-429	2.54	0.04	$7.23 \cdot 10^{-10}$
4U1705-44	8.04	0.12	$2.28 \cdot 10^{-9}$

Table 8 *continued on next page*

Table 8 (*continued*)

Source	ASM Counts	Flux density	Flux 2-10 keV
	sec ⁻¹	mJy at 5 keV	ergs cm ⁻² s ⁻¹
GX9+9	25.93	0.38	$7.37 \cdot 10^{-9}$
GX354+0	6.320	0.09	$1.80 \cdot 10^{-9}$
4U1735-444	11.90	0.17	$3.38 \cdot 10^{-9}$
GX 3+1	26.88	0.39	$7.64 \cdot 10^{-9}$
GX 9+1	36.18	0.53	$1.03 \cdot 10^{-8}$
GX 13+1	21.88	0.32	$6.20 \cdot 10^{-9}$
Aql X-1	<0.01		
Pulsars			
SMC X-3	<0.01		
SMC X-1	2.368	0.03	$6.73 \cdot 10^{-10}$
Vela X-1	3.79	0.06	$1.08 \cdot 10^{-9}$
Cen X-3	1.81	0.03	$5.14 \cdot 10^{-10}$
GX 301-2	1.10	0.16	$3.12 \cdot 10^{-10}$
4U1538-522	1.60	0.02	$4.55 \cdot 10^{-10}$
4U1700-37	5.26	0.08	$1.49 \cdot 10^{-9}$
GX 1+4	<0.01		
Swift J1756.9-2508	<0.01		
4U1822-37	1.56	0.22	$4.43 \cdot 10^{-10}$
4U1907+097	1.67	0.24	$4.75 \cdot 10^{-10}$

The All Sky Monitor (ASM; [Levine et al. 1996](#)) on board NASA’s Rossi X-ray Timing Explorer (RXTE) operated continuously for nearly 15 years (1996-2012). It consisted of three wide-angle shadow cameras equipped with proportional counters with a total collecting area of 90 cm². It had an energy range of 2-10 keV and covered 80% of the sky every 90 minutes with a sensitivity of 30 mCrab. The MIT ASM ⁶ team provides data in three energy bins (1.3-3.0, 3.0-5.0, and 5.0-12.0 keV) sampled 4-8 times a day, as well as one-day averages. The 14-year lightcurves with the week of our observations highlighted are plotted in the Appendix (Sec. A) to show the context of this campaign in the history of each source. Averages of the X-ray flux of individual sources were extracted for each day of our campaign. Only detections of 3 sigma or greater were accepted. The 1.3-12 keV energy band count rates were averaged over the week of the campaign to represent the intensity of the source, shown on Table 8. The count rates were converted to flux density in Crabs by conversion factor 75 ASM counts sec⁻¹ equals 1 Crab. For the SEDs, the flux density (in Jy) was determined from the formula 1 Crab at 5 keV is 1.088 mJy⁷. For the SEDs (section 3 below), values are plotted at frequency corresponding to 5 keV = $1.21 \cdot 10^{18}$ Hz.

2.5.3. RXTE PCA

All PCA observations collected data in two standard modes, Standard1, with a time resolution of 0.125s and no energy information, and Std2 with a time resolution of 16s and 129 energy channels (numbered 0-128) from the full energy range. Our analysis used the Standard2 data files, backgrounds, and responses, downloaded from NASA’s High Energy Archive Research Center (HEASARC). Inspection of background light curves showed that the Standard mode extractions did not need to be revised, although for the dim source LMC X-3 we adjusted the scale of the background.

⁶ http://xte.mit.edu/ASM_lc.html

⁷ https://space.mit.edu/~jonathan/xray_detect.html

Table 9. RXTE PCA: Model components for each source, black holes fit with powerlaw and diskBB

Name	Start MJD	Exp. (s)	N_H 10^{22} cm^{-2}	Power Law		diskBB		χ^2 per d.o.f.
				γ	norm	T_{in} keV	norm	
LMC X-3	54280.211- 54287.237	22926	0.03	$1.9^{+0.1}_{-0.5}$	$2.6 \pm 0.1 \times 10^{-3}$... ^a	...	37.6/42
GX 339-4	54280.101- 54287.237	10160	0.51	$1.3^{+0.1}_{-0.2}$	$0.10^{+0.01}_{-0.05}$	$1.7^{+0.9}_{-0.3}$	2 ± 2	51/37
GRS 1915+105	54286.124	1536	3 ± 2	2.29 ± 0.04	70 ± 10	3.8 ± 0.1	180^{+50}_{-40}	52.9/39
4U 1957+11	54282.593	6304	0.08^b	-1.6 ± 1.8	$1 \times 10^{-7} (< 2 \times 10^{-5})$	1.39 ± 0.01	13.4 ± 0.7	38.3/40

^aThere is no evidence for a diskBB component.

^bThis variable fixed not fitted, to match the XRT value.

We fit the spectra using XSPEC (Arnaud 1996). We fit neutron star systems with a model of a Comptonized hard spectrum (Titarchuk 1994, COMPTT), plus a multicolor disk blackbody (DISKBB, Makishima et al. 1986), absorbed by a column density usually set to that either found by contemporaneous Swift observations or expected from interstellar gas along the sightline (calculated from HI data). For the absorbing component we used the TBabs model, based on Wilms et al. (2000). In some cases to obtain an acceptable fit (with $\chi^2_\nu < 2$) we allowed the interstellar absorbing column to vary. In some cases we included a Gaussian emission line near 6.4 keV. For 4U 1907+09, we included a cyclotron absorption line. For Sco X-1, we allowed a systematic error of 0.25

Errors on fluxes were determined using the XSPEC cflux multiplicative model component. In cases where this returned only the errors on the unabsorbed flux of model components, we scaled those errors to apply to the absorbed fluxes. Where power law, Comptonized, or disk blackbody components were absorbed not only by interstellar gas but by a cyclotron feature, we report the flux after the model component has been subject to multiplication by the cyclotron feature. Resulting model parameters are given on Table 9 for black holes, and 10 for neutron stars, and Table 11 gives the resulting fluxes (absorbed and unabsorbed). Tables 9 and 10 include break-downs for the disk black-body contribution and the contributions of power law or Comptonization components.

Table 10. RXTE PCA: Model components for each source, neutron stars fit with compTT and diskBB

			CompTT			diskBB			
Start	Exp	N_H (10^{22})	T_0	kT	τ_p	norm	T_{in}	norm	χ^2
MJD	s	cm^{-2}	keV	keV					per d.o.f.
Z Sources									
Sco X-1									
54280.172	1344
54284.441	1104
Average	...	0.30	$1.0^{+0.1}_{-0.9}$	3.0 ± 0.03	5.7 ± 0.3	8 ± 7	1.2 ± 0.2	$<10^4$	62.2/37

Table 10 continued on next page

Table 10 (*continued*)

		CompTT				diskBB			
Start	Exp	N _H (10 ²²)	T ₀	kT	τ _p	norm	T _{in}	norm	χ ²
MJD	s	cm ⁻²	keV	keV					per d.o.f.
XTE J1701-461									
Average 54280.000- 54285.633	4944	2.1	1.18 ^{+0.02} _{-0.1}	6 < 50	< 7 [†]	...	3.21 ^{+0.08} _{-0.04}	0.17 ^{+0.1} _{-0.7}	39.1/37
GX 349+2									
54286.453	2704	0.7	1.0 ⁺¹ _{-0.1}	< 70	< 20	> 0.02	2.9±0.1	7 ⁺² ₋₁	56.3/36
GX 17+2									
54285.668	3104	2.16	0.001	2.6±0.2	200 [†]	0.2±4	1.64 ^{+0.04} _{-0.02}	174±1	70.9/44
Atoll Sources									
EXO 0748-676									
Average 54286.531- 54286.844	9088	0.101	1.2 ⁺⁵ _{-0.3}	< 70	0.01 ^{†a}	< 0.8	7.8 ⁺¹ _{-0.3}	7 ⁺¹ ₋₂ × 10 ⁻³	36.0/44
4U 1254-690									
54280.348	6000	2 ⁺³ ₋₁	0.001	2.4 ^{0.2} _{-0.1}	(> 100)	> 0.0086	1.6±0.1	8±2	36.5/37
4U 1608-52									
54280.449	1072	0.84	0.96±0.01	2.77 ^{+0.04} _{-0.04}	4.7 ^{+0.2} _{-0.2}	0.67 ^{+0.03} _{-0.02}	35.8/38
54280.766	1104	0.84	8±8	2.20 ^{+1.4} _{-0.04}	>50	0.4 ⁺² _{-0.2}	1.96±0.03	34±2	37.2/38
54285.730	1680	0.84	7 (<13)	2.1 ^{+1.0} _{-0.05}	200 [†]	0.4 ^{+1.2} _{-0.2}	2.12±0.05	25±3	36.8/38
4U 1636-53									
54285.731	3200	0.26	0.95±0.02	2.44 ^{+0.05} _{-0.04}	5.0±0.2	0.75 ^{+0.03} _{-0.04}	< 0.9	...	34.0/38
4U 1705-44									
54284.488	2688	0.808	0.001	< 3	> 180	< 30	1.60±0.01	> 30	47.2/36
54280.645	2912	0.808	< 20	2.54 ⁺² _{-0.1}	200 [†]	< 1	1.88±0.02	12.1±0.1	30.4/35
average	...	0.808	1.0 ^{+0.2} _{-0.3}	2.6±0.1	6 ⁺⁴ ₋₁	0.2±0.1	1.3 ^{+0.2} _{-1.3}	< 2000	58.7/ 36
GX 9+9									
54285.730	3200	0.21	7.11±0.06	2.09 ^{+0.01} _{-0.08}	200 [†]	< 0.4	1.89±0.01	39±1	43.4/38
4U 1735-444									
Average 54280.699- 542825.273	25984	0.3	1.02±0.02	2.8±0.1	7 ⁺⁵ ₋₁	0.2±0.2	> 0.2	16±3	25.2/38
Aql X-1									
54281.223	1184	0.45	0.7±0.2	470 ⁺³⁰ ₋₁₄₀	0.03 ^{+0.02} _{-0.01}	6±2(-5)	44.4/ 40
54282.133	1264	0.63	< 1	< 200	2.5 ⁺¹⁴ _{-2.1}	< 0.01	25.4/40
54283.516	2128	0.63	< 1.3	20 ⁺¹⁰⁰ ₋₁₀	< 5	< 0.002	39.1/40
54284.230	1104	0.63	< 2.3	500±50	< 100	< 0.02	13.1/40 ^c
54285.145	1072	0.96	< 5	> 200	< 200	< 0.1	23.4/40
Pulsars									
4U 1907+09 ^b									
54282.398	1904	1.70	90	5.9 ^{+1.5} _{-0.5}	200 [†]	35 ⁺⁵⁰ ₋₃₀	3.7 ^{+0.8} _{-0.2}	0.11 ^{+0.2} _{-0.05}	34.0/34

Table 10 continued on next page

Table 10 (*continued*)

Start	Exp	N_H (10^{22})	CompTT				diskBB		χ^2
			T_0	kT	τ_p	norm	T_{in}	norm	
MJD	s	cm^{-2}	keV	keV					per d.o.f.
54284.363	1920	1.70	0.001	30 ± 10	200^\dagger	< 0.1	2 ± 1	< 0.5	23.2/35
54281.223	1760	1.70	< 1.4	20_{-10}^{+100}	3 ± 3	< 0.08	\dots	\dots	32.6/39
Average	\dots	1.70	85	7_{-2}^{+1}	200^\dagger	7.1_{-7}^{+12}	$3.7_{-0.1}^{+0.5}$	$0.05_{-0.02}^{+0.06}$	30.2/34

^a \dagger indicates that the best fit is with this parameter at the edge of its allowed range.

^b This source contains a cyclotron line. Leaving the parameters of the cyclotron line free along with the compTT high energy component of the spectrum results in T_0 for compTT being very poorly constrained.

^c The low value of χ^2 results from large error bars on the spectrum.

2.5.4. *Swift* BAT observations

The Burst Alert Telescope (BAT) is a highly sensitive, wide field, coded aperture imaging instrument with a 1.4 steradian field-of-view (half coded) with CdZnTe detectors. The energy range is 15 – 150 keV for imaging with a non-coded response up to 500 keV, but here we use only 15-50 keV as the higher energy values are less reliable. We divide the flux in this energy range by the bandwidth to get the flux density at the nominal band center of 32.5 keV. Further information on the BAT is given by [Barthelmy et al. \(2005\)](#). For the model a nominal column density of $1 \times 10^{21} \text{ cm}^{-2}$ is used for N_H ⁸, and a power-law with index=1.5 for the emission spectrum. This provides a flux in $\text{ergs cm}^{-2} \text{ s}^{-1}$, that is converted to a flux density by dividing by the bandwidth in Hz. For the SEDs (section 3 below) the values are plotted at the central energy of 32.5 keV which corresponds to $7.86 \cdot 10^{18} \text{ Hz}$. Flux densities and upper limits from the BAT are given on Table 12.

⁸

For these energy bands the estimated flux is insensitive to absorption. At $1 \times 10^{21} \text{ cm}^{-2}$ there is no difference between the absorbed and unabsorbed fluxes. For $1 \times 10^{24} \text{ cm}^{-2}$ the difference between the absorbed and unabsorbed fluxes is only 2%.

Table 11. RXTE PCA: Fluxes, absorbed and unabsorbed

Source	Date	Total 2-10 keV	Total 10-20 keV	Total, $N_H=0$ 2-10 keV	diskBB 2-10 keV	10-20 keV	$N_H=0$ 2-10 keV ^b	PL ^a 2-10 keV	10-20 keV	$N_H=0$ 2-10 keV
Black Holes										
LMC X-3	all	$1.8 \pm 8 \times 10^{-11}$	$3.8 \pm 0.4 \times 10^{-12}$	$1.8 \pm 8 \times 10^{-11}$	$< 4 \times 10^{-10}$	$< 6 \times 10^{-10}$	$< 4 \times 10^{-10}$	$7 \pm 1 \times 10^{-12}$	$3.8 \pm 0.4 \times 10^{-12}$	$7 \pm 1 \times 10^{-12}$
GX 339-4	all	$7.6^{+0.4}_{-0.3} \times 10^{-10}$	$7.49 \pm 0.06 \times 10^{-10}$	$1.3 \pm 0.1 \times 10^{-9}$	$2.9 \pm 0.6 \times 10^{-10}$	$4 \pm 2 \times 10^{-11}$	$5 \pm 1 \times 10^{-10}$	$4.7 \pm 0.5 \times 10^{-10}$	$7.1 \pm 0.2 \times 10^{-10}$	$7.5 \pm 0.8 \times 10^{-10}$
GRS 1915+105	54285	$4.7^{+0.4}_{-0.3} \times 10^{-8}$	$5.29 \pm 0.03 \times 10^{-9}$	$6.8 \pm 0.4 \times 10^{-8}$	$5.39 \pm 0.03 \times 10^{-9}$	3.7×10^{-9}	$2.7 \pm 0.1 \times 10^{-8}$	$2.5 \pm 0.1 \times 10^{-8}$	1.59×10^{-9}	$4.1 \pm 0.2 \times 10^{-8}$
4U 1957+11	all	$6.38 \pm 0.09 \times 10^{-10}$	$1.6^{+0.03}_{-0.1} \times 10^{-11}$	$6.44 \pm 0.09 \times 10^{-10}$	$1.6^{+0.03}_{-0.1} \times 10^{-11}$	$1.40 \pm 0.05 \times 10^{-11}$	$6.44 \pm 0.09 \times 10^{-10}$	$2^{+12}_{-1} \times 10^{-13}$	$2 \pm 1 \times 10^{-12}$	$2^{+12}_{-1} \times 10^{-13}$
Z Sources										
Sco X-1	all	$1.172^{+0.004}_{-0.002} \times 10^{-7}$	$3.115 \pm 0.004 \times 10^{-8}$	$1.20^{+0.03}_{-0.02} \times 10^{-7}$	$3.120 \pm 0.003 \times 10^{-8}$	$1.91^{+0.04}_{-0.05} \times 10^{-8}$	$2.00 \pm 0.05 \times 10^{-8}$	$1.0 \pm 0.1 \times 10^{-7}$	$3.10^{+0.01}_{-0.04} \times 10^{-8}$	$1.0 \pm 0.1 \times 10^{-7}$
XTE J1701-461	all	$3.31^{+0.03}_{-0.03} \times 10^{-9}$	$8.69 \pm 0.04 \times 10^{-10}$	$3.85^{+0.03}_{-0.03} \times 10^{-9}$	$8.69 \pm 0.04 \times 10^{-10}$	$2.09^{+0.06}_{-0.06} \times 10^{-9}$	$2.41^{+0.06}_{-0.06} \times 10^{-9}$	$1.2^{+0.6}_{-0.1} \times 10^{-9}$	$5^{+20}_{-0.1} \times 10^{-11}$	$1.4^{+2}_{-0.1} \times 10^{-9}$
GX 349+2	54286	$1.32^{+0.03}_{-0.02} \times 10^{-8}$	$2.51 \pm 0.01 \times 10^{-9}$	$1.39^{+0.03}_{-0.02} \times 10^{-8}$	$2.52 \pm 0.01 \times 10^{-9}$	$6.7^{+0.1}_{-0.1} \times 10^{-9}$	$7.1^{+0.1}_{-0.5} \times 10^{-9}$	$6.1 \pm 0.3 \times 10^{-9}$	$5.9^{+1.3}_{-0.5} \times 10^{-10}$	$6.5 \pm 0.3 \times 10^{-9}$
GX 17+2	54285	$1.64 \pm 0.03 \times 10^{-8}$	$2.82 \pm 0.01 \times 10^{-9}$	$2.00^{+0.03}_{-0.03} \times 10^{-8}$	$2.86 \pm 0.01 \times 10^{-9}$	1.4×10^{-8}	7.8×10^{-10}	2.0×10^{-9}	2.0×10^{-9}	2.8×10^{-9}
Atoll Sources										
EXO 0748-676	all	$2.45^{+0.07}_{-0.04} \times 10^{-10}$	$1.80 \pm 0.01 \times 10^{-10}$	$2.45^{+0.07}_{-0.04} \times 10^{-10}$	$1.80 \pm 0.01 \times 10^{-10}$	$1.67^{+0.05}_{-0.40} \times 10^{-10}$	$1.67^{+0.05}_{-0.40} \times 10^{-10}$	$8.0^{+0.4}_{-0.3} \times 10^{-11}$	$4^{+20}_{-1} \times 10^{-12}$	$8.0^{+0.4}_{-0.3} \times 10^{-11}$
4U 1254-690	54280	$7 \pm 1 \times 10^{-10}$	$1.2 \pm 0.2 \times 10^{-10}$	$8.5^{+0.1}_{-0.1} \times 10^{-10}$	$1.21 \pm 0.04 \times 10^{-10}$	5.6×10^{-10}	2.9×10^{-11}	$1.3 > 0.2 \times 10^{-10}$	9.1×10^{-11}	$1.4 \pm 0.2 \times 10^{-10}$
4U 1608-52	54280	$6.6 \pm 0.2 \times 10^{-9}$	$1.25 \pm 0.01 \times 10^{-9}$	$7.0^{+0.4}_{-0.1} \times 10^{-9}$	$1.26 \pm 0.01 \times 10^{-9}$	$< 3 \times 10^{-10}$	8×10^{-13}	$6 \pm 1 \times 10^{-9}$	$1.25 \pm 0.01 \times 10^{-9}$	$6.5 \pm 1.0 \times 10^{-9}$
4U 1608-52	54280	$7.0 \pm 0.1 \times 10^{-9}$	$1.22 \pm 0.01 \times 10^{-9}$	$7.5 \pm 0.1 \times 10^{-9}$	$1.23 \pm 0.01 \times 10^{-9}$	$6.7 \pm 0.1 \times 10^{-9}$	$7.3 \pm 0.1 \times 10^{-9}$	$2.6^{+0.6}_{-0.2} \times 10^{-10}$	$5.6^{+0.4}_{-0.2} \times 10^{-10}$	$2.7^{+0.6}_{-0.2} \times 10^{-10}$
4U 1608-52	54281	$7.2 \pm 0.1 \times 10^{-9}$	$1.58 \pm 0.01 \times 10^{-9}$	$7.8 \pm 0.1 \times 10^{-9}$	1.6×10^{-9}	$6.77 \pm 0.04 \times 10^{-9}$	$7.69 \pm 0.04 \times 10^{-9}$	$3.9^{+0.6}_{-0.6} \times 10^{-10}$	$7.2^{+0.6}_{-0.6} \times 10^{-10}$	4.0×10^{-10}
4U 1636-53	all	$6.5 \pm 0.1 \times 10^{-9}$	$9.52^{+0.05}_{-0.04} \times 10^{-10}$	$6.6 \pm 0.1 \times 10^{-9}$	$9.52^{+0.05}_{-0.04} \times 10^{-10}$	$6.5 \pm 0.1 \times 10^{-9}$
4U 1705-44	54280	$3.55 \pm 0.01 \times 10^{-9}$	$6.36 \pm 0.02 \times 10^{-10}$	$3.84 \pm 0.01 \times 10^{-9}$	$6.40 \pm 0.01 \times 10^{-10}$	2.7×10^{-9}	3.0×10^{-9}	1.1×10^{-9}	5.2×10^{-10}	8.5×10^{-10}
4U 1705-44	54284	$2.2 \pm 0.1 \times 10^{-9}$	$4.0 \pm 0.1 \times 10^{-10}$	$2.4 \pm 0.2 \times 10^{-9}$	$4.1 \pm 0.1 \times 10^{-10}$	$2.00 \pm 0.01 \times 10^{-9}$	$2.16 \pm 0.01 \times 10^{-9}$	$1.8^{+0.6}_{-0.6} \times 10^{-10}$	$2.35^{+0.6}_{-0.6} \times 10^{-10}$	$1.9^{+0.6}_{-0.6} \times 10^{-10}$
4U 1705-44	all	$2.7 \pm 0.1 \times 10^{-9}$	$5.2 \pm 0.3 \times 10^{-10}$	$2.9 \pm 0.1 \times 10^{-9}$	$5.2 \pm 0.3 \times 10^{-10}$	$6.2 \pm 0.2 \times 10^{-10}$	$6.9 \pm 0.3 \times 10^{-10}$	$2.0 \pm 0.1 \times 10^{-9}$	$5.1^{+0.1}_{-0.1} \times 10^{-10}$	$2.2 \pm 0.1 \times 10^{-9}$
GX 9+9	54285	$7.2 \pm 0.1 \times 10^{-9}$	$9.5^{+0.7}_{-0.3} \times 10^{-10}$	$7.4 \pm 0.14 \times 10^{-9}$	$9.5 \pm 0.1 \times 10^{-10}$	$7.01 \pm 0.04 \times 10^{-9}$	$7.16 \pm 0.04 \times 10^{-9}$	$2.3^{+0.7}_{-0.3} \times 10^{-10}$	$3.8^{+0.5}_{-0.3} \times 10^{-10}$	$2.3^{+0.7}_{-0.3} \times 10^{-10}$
4U 1735-444	all	$3.2^{+0.5}_{-0.1} \times 10^{-9}$	$1.02 \pm 0.01 \times 10^{-9}$	$3.3 \pm 0.2 \times 10^{-9}$	$1.02 \pm 0.01 \times 10^{-9}$	7.3×10^{-10}	7.6×10^{-10}	$2.5(> 1.5) \times 10^{-9}$	$1.0 \pm 0.1 \times 10^{-9}$	$2.5(> 1.5) \times 10^{-9}$
Aql X-1	54281	$9.5 \pm 1.1 \times 10^{-11}$	$5.7^{+0.4}_{-0.2} \times 10^{-11}$	$9.9 \pm 1.2 \times 10^{-11}$	5.7×10^{-11}	$9.5 \pm 1.1 \times 10^{-11}$	$5.7^{+0.4}_{-0.2} \times 10^{-11}$	$9.5 \pm 1.1 \times 10^{-11}$
Aql X-1	54282	$5.3 \pm 0.5 \times 10^{-11}$	$3.7 \pm 0.2 \times 10^{-11}$	$5.6^{+0.7}_{-0.6} \times 10^{-11}$	$3.8^{+0.2}_{-0.3} \times 10^{-11}$	$5.3 \pm 0.5 \times 10^{-11}$	$3.7 \pm 0.2 \times 10^{-11}$	$5.6^{+0.7}_{-0.6} \times 10^{-11}$
Aql X-1	54283	$1.5^{+0.3}_{-0.2} \times 10^{-11}$	$1.7 \pm 0.2 \times 10^{-11}$	$1.6^{+0.3}_{-0.3} \times 10^{-11}$	$1.7 \pm 0.2 \times 10^{-11}$	$1.5^{+0.3}_{-0.2} \times 10^{-11}$	$1.7 \pm 0.2 \times 10^{-11}$	$1.6^{+0.3}_{-0.2} \times 10^{-11}$
Aql X-1	54284	$5.7 \pm 0.2 \times 10^{-12}$	$8.8 \pm 0.1 \times 10^{-12}$	$5.9^{+0.3}_{-0.3} \times 10^{-12}$	$8.8 \pm 0.1 \times 10^{-12}$	$5.7 \pm 0.2 \times 10^{-12}$	$8.8 \pm 0.1 \times 10^{-12}$	$5.9^{+0.3}_{-0.3} \times 10^{-12}$
Aql X-1	54285	$3.7^{+2}_{-1} \times 10^{-12}$	$6 \pm 1 \times 10^{-12}$	$3.9^{+4}_{-3} \times 10^{-12}$	$6^{+2}_{-1} \times 10^{-12}$	$3.7^{+2}_{-1} \times 10^{-12}$	$6 \pm 1 \times 10^{-12}$	$3.9^{+4}_{-3} \times 10^{-12}$
Pulsars										
4U 1907+09	54280	$2.32 \pm 5 \times 10^{-10}$	$1.5^{+0.3}_{-0.1} \times 10^{-10}$	$2.6 \pm 0.1 \times 10^{-10}$	$1.6^{+0.3}_{-0.1} \times 10^{-10}$	$1.8 \pm 0.1 \times 10^{-10}$	$2.1 \pm 0.1 \times 10^{-10}$	$3 \pm 1 \times 10^{-11}$	$1.3^{+0.3}_{-0.3} \times 10^{-10}$	$3 \pm 1 \times 10^{-11}$
4U 1907+09	54282	$3.8^{+0.2}_{-0.4} \times 10^{-11}$	$1.8^{+0.4}_{-0.1} \times 10^{-11}$	$4.2 \pm 0.3 \times 10^{-11}$	$1.8^{+0.7}_{-0.1} \times 10^{-11}$	$2.1^{+0.4}_{-0.3} \times 10^{-11}$	$3.1^{+0.4}_{-0.3} \times 10^{-11}$	$8.4 \pm 0.5 \times 10^{-12}$	$1.8 \pm 0.8 \times 10^{-11}$	$1.1 > 0.6 \times 10^{-11}$
4U 1907+09	54285	$1.7^{+0.4}_{-0.4} \times 10^{-11}$	$1.8 \pm 0.3 \times 10^{-12}$	$2.0 \pm 0.6 \times 10^{-11}$	$1.8 \pm 0.3 \times 10^{-12}$	0	0	$1.7^{+0.4}_{-0.4} \times 10^{-11}$	$1.8 \pm 0.3 \times 10^{-12}$	$2.0 \pm 0.6 \times 10^{-11}$
4U 1907+09	all	$1.11^{+0.14}_{-0.03} \times 10^{-10}$	$6.8^{+2}_{-0.3} \times 10^{-11}$	$1.24^{+0.16}_{-0.04} \times 10^{-10}$	$6.9^{+2}_{-0.1} \times 10^{-11}$	$1.1^{+0.08}_{-0.02} \times 10^{-10}$	$1.24^{+0.08}_{-0.02} \times 10^{-10}$	$2.2^{+3}_{-0.5} \times 10^{-11}$	$7.6^{+1.4}_{-6.6} \times 10^{-10}$	$2.3^{+3}_{-0.5} \times 10^{-11}$

^a PL is power law or Comptonization component

^b The $N_H=0$ corrections for 10-20 keV band in the separate components are small, and similar to the correction to the total flux.

Table 12. Swift BAT Results

Source	BAT Counts sec ⁻¹	Flux at 31.5 keV ergs cm ⁻² s ⁻¹
Black Holes		
LMC X-3	<0.01	<1.0×10 ⁻¹⁰
LMC X-1	<0.01	<1.0×10 ⁻¹⁰
XTE J1550-564	<0.01	<1.0×10 ⁻¹⁰
4U1630-47	<0.01	<1.0×10 ⁻¹⁰
GROJ1655-40	<0.01	<1.0×10 ⁻¹⁰
GX339-4	0.0063	6.49×10 ⁻¹¹
1E 1740-29	0.0032	3.30×10 ⁻¹¹
GRS 1758-258	0.0054	5.56×10 ⁻¹¹
V4641 SGR	<0.01	<1.0×10 ⁻¹⁰
GRS1915+105	0.035	3.63×10 ⁻¹⁰
4U1957+115	<0.0023	<2.4×10 ⁻¹¹
Z Sources		
LMC X-2	<0.01	<1.0×10 ⁻¹⁰
Cir X-1	<0.01	<1.0×10 ⁻¹⁰
Sco X-1	0.3575	3.68×10 ⁻⁹
GX340+0	<0.01	<1.0×10 ⁻¹⁰
XTE J1701-462	0.0058	5.98×10 ⁻¹¹
GX349+2	0.018	1.85×10 ⁻¹⁰
GX 5-1	0.028	2.84×10 ⁻¹⁰
GX 17+2	0.0142	1.46×10 ⁻¹⁰
Atoll Sources		
EXO 0748-67	0.0088	9.07×10 ⁻¹¹
4U1254-69	<0.0033	< 9.1×10 ⁻¹¹
Cen X-4	<0.01	<1.0×10 ⁻¹⁰
4U1543-624	<0.01	<1.0×10 ⁻¹⁰
4U1608-522	0.0074	7.63×10 ⁻¹¹
4U1636-53	0.0082	8.45×10 ⁻¹¹
4U1658-298	<0.01	<1.0×10 ⁻¹⁰
4U1702-429	0.0026	2.68×10 ⁻¹¹
4U1705-44	0.0023	2.37×10 ⁻¹¹
GX9+9	0.0066	6.80×10 ⁻¹¹
GX354+0	0.0176	1.81×10 ⁻¹⁰
4U1735-444	0.0082	8.45×10 ⁻¹¹
GX 3+1	0.0062	6.39×10 ⁻¹¹
GX 9+1	0.0071	7.32×10 ⁻¹¹
GX 13+1	0.0035	3.61×10 ⁻¹¹
Aql X-1	<0.01	<1.0×10 ⁻¹⁰

Table 12 *continued on next page*

Table 12 (*continued*)

Source	BAT Counts sec ⁻¹	Flux at 31.5 keV ergs cm ⁻² s ⁻¹
Pulsars		
SMC X-3	<0.01	<1.0×10 ⁻¹⁰
SMC X-1	<0.002	<2.27×10 ⁻¹¹
Vela X-1	0.0706	7.28×10 ⁻¹⁰
Cen X-3	0.0144	1.48×10 ⁻¹⁰
GX 301-2	0.0451	4.65×10 ⁻¹⁰
4U1538-522	0.0054	5.56×10 ⁻¹¹
4U1700-37	0.0269	2.77×10 ⁻¹⁰
GX 1+4	0.0173	1.78×10 ⁻¹⁰
Swift J1756.9-2508	<0.01	<1.0×10 ⁻¹⁰
4U1822-37	0.0084	8.66×10 ⁻¹¹
4U1907+097	0.0049	5.05×10 ⁻¹¹

3. SPECTRAL ENERGY DISTRIBUTIONS

Here we summarize the results and interpret the SEDs of each of the X-ray binaries observed. While most sources have detections at multiple wavelengths during the week of our campaign, we only plot the SEDs of those that had at least one X-ray spectrum, rather than just single frequency observations. Overall, 23 individual sources have X-ray spectra: 16 from 2-20 keV obtained with the RXTE PCA, and 16 from 0.2 to 10 keV obtained with the Swift XRT, with 9 detected by both instruments.

To determine the states of individual sources during our week of observations we obtained the XTE Mission-Long Source Catalog file ⁹ for each source from the HEASARC archive ¹⁰, when available. Each row in the file is a separate RXTE observation (obsid), drawn from all proposals that included the source as a target. For each observation this gives the time of the observation, PCU Std 2 data rates (in three bands: 2-4 keV, 4-9 keV, 9-20 keV), and errors. The PCA data are normalized to 1 PCU (ie., rates are in units of c/s/PCU). There is a single value for each pointed RXTE observation. For sources for which these files exist we created a color-intensity (CI) plot for each source by summing the three bands and determining an X-ray color or hardness ratio (HR, normalized to ± 1) from the 2-4 keV and 9-20 keV bands. The X-ray color is expressed as a ratio of the difference divided by the sum of bands at 9-20 keV (p920) and 2-4 keV (p24). The color is shown on the x-axis, while the intensity over the full range 2 to 20 keV is plotted on the y-axis. When Mission-Long Source Catalog files are not available for a source the CI diagrams are made using RXTE ASM data which are provided in three energy bands: a (1.5-3 keV), b (3-5 keV), and c (5-12 keV). Color is determined using bands a and c, and intensity is determined by the sum of all three bands. RXTE observations (either PCA or ASM) made during our week of observations are denoted in red. Blue points indicate the range of values measured for the source at other epochs using the same instrument.

Sources are described as persistent if they are continuously active and transient if they have periods of quiescence when little or no emission is detected. Persistent sources can be variable, i.e. show changes in intensity, or steady, i.e. show a nearly constant count rate. ASM light curves for all sources for most of the 15 years that the RXTE was active are shown in Sec. A.

3.1. Black holes (11 sources; 6 with SEDs)

LMC X-3 (4U 0538-64; Fig. 9) is a persistent, variable source with a high mass companion star. It is found mainly in a soft X-ray state with rare excursions into hard state (Bhuvana et al. 2021). During the week of our campaign it was at very low X-ray flux (blue arrows in Fig. 32.28.). It gives upper limits in the ATCA data. It was not observed

⁹ https://heasarc.gsfc.nasa.gov/docs/xte/recipes/mllc_start.html

¹⁰ <https://heasarc.gsfc.nasa.gov/cgi-bin/W3Browse/w3browse.pl>

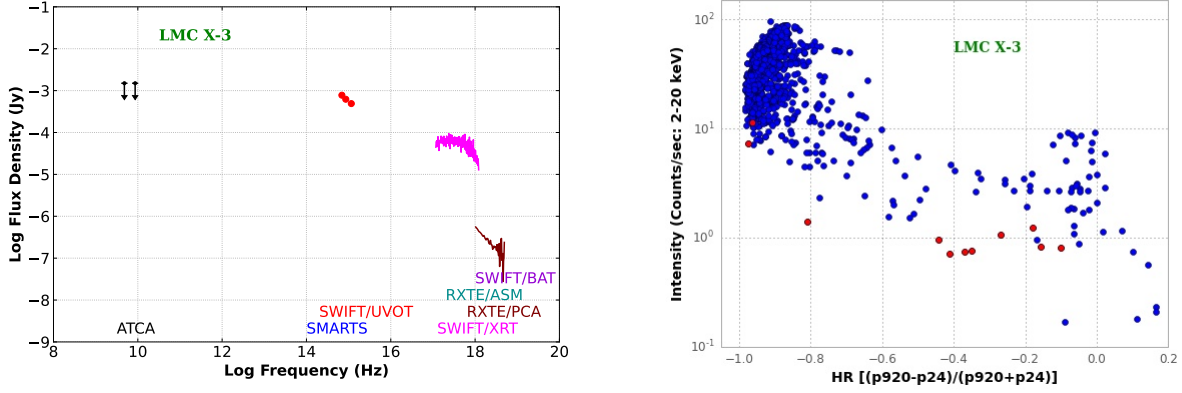


Figure 9. Left panel: spectral energy distribution of LMC X-3. The y-axis is the \log_{10} of the flux density in Jy and the x-axis is \log_{10} of the frequency in Hz. The various instruments contributing are indicated across the bottom with colors matching the corresponding data. Right panel: the color-intensity (CI) plot for LMC X-3 using RXTE/PCA data. The X-ray color expressed as a ratio of the difference divided by the sum of bands at 9-20 keV (p920) and 2-4 keV (p24) is shown on the x-axis, while the intensity over the full range 2 to 20 keV is plotted on the y-axis. The red points indicate the values obtained for the week of the campaign, and the blue points indicate the range of values measured for the source at other epochs.

by SMARTS. No significant detections were made with the Swift BAT during the week of the campaign. While there is no Swift XRT data during the week of the campaign we have included a spectrum taken 12 days later (green arrows in Fig. 32.28.) when the source was rising in flux (first entry on Table 6). The significant discrepancy between the XRT and PCA spectra taken a few days apart demonstrates the need for simultaneous, multiwavelength observations when observing XRBs. The CI diagram (Fig. 9 right panel) constructed with PCA data shows that the source was in the faint intermediate state (segment labeled D in Fig. 1). No radio emission is expected in the D state, consistent with the upper limit found by the ATCA.

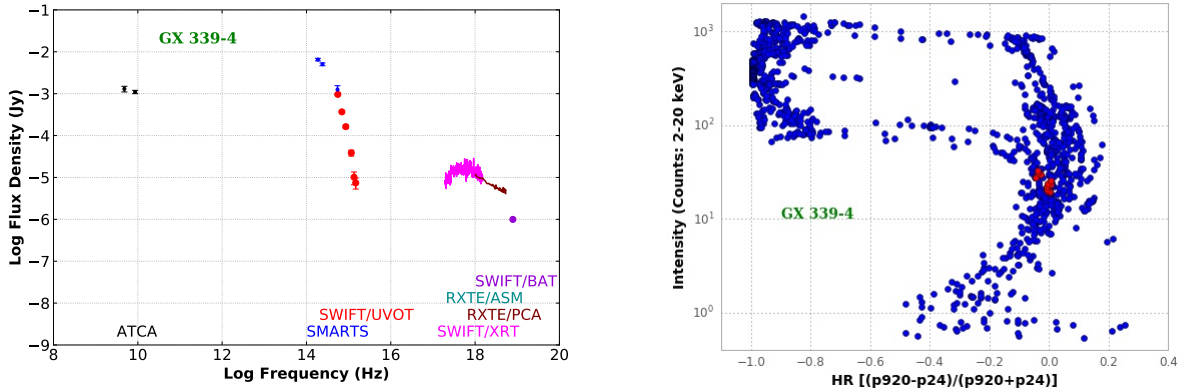


Figure 10. Spectral Energy Distribution and color-intensity plots of GX 339-4. The X-ray spectra are from obsid 00030953005 on Table 6 (SWIFT/XRT) and the time average shown on Table 9 (RXTE/PCA). The panels and colors are as in figure 9.

GX 339-4 (4U 1659-487; V821 Ara; Fig. 10; Fig. 32.19.) is an X-ray transient caught in the lower part of the low/hard state. It is a dipping source implying a relatively high inclination angle (Sasano et al. 2014). There are ATCA detections at the mJy level. There are detections by SMARTS, Swift UVOT, Swift XRT, RXTE PCA, and Swift BAT. There is no significant detection by the RXTE ASM during the week of the campaign. The PCA CI diagram shows that the source is at the cusp between C, D, and E states on Fig. 1. The radio detection implies that the flat-spectrum, compact radio source is present, as expected in the C and E states. The Swift BAT points suggest a sharp cutoff around 20 to 30 keV.

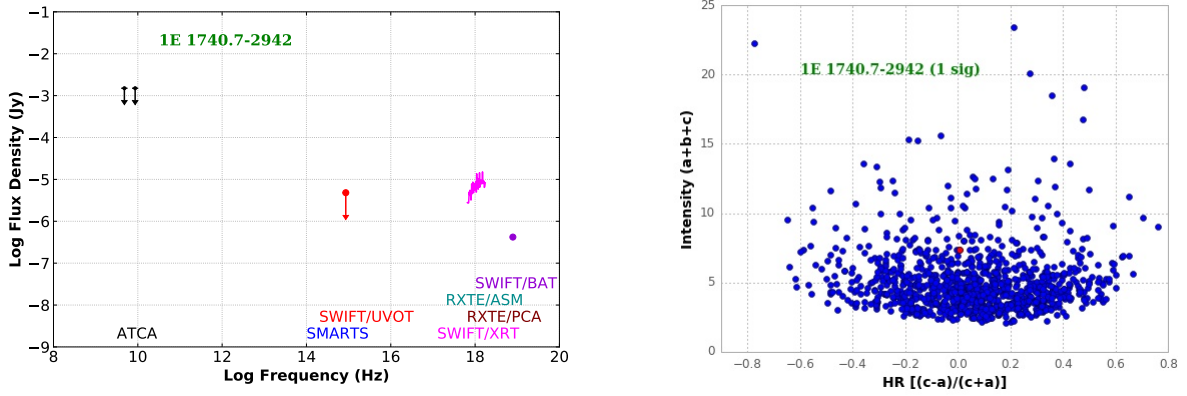


Figure 11. Spectral Energy Distribution and CI plots of 1E 1740.7-2942 using RXTE/ASM data. The left panel axes are as in figure 9. The right panel has color (hardness ratio) defined using the ASM bands c (5-12 keV) and a (1.5-3 keV), and intensity using the sum of ASM bands a, b, and c (1.5-12 keV). The red point indicates the values during the campaign, and the blue points indicate the range of values measured for the source at other epochs.

1E 1740.7-2942 (Great annihilator; Fig. 11; Fig. 32.12.) is a persistent, low flux source. Although it is known to show radio lobe structure and clear jet-ISM interaction (Tetarenko et al. 2020; Saavedra et al. 2022), during this campaign there are only upper limits with the ATCA. There is also only one detection by the RXTE ASM, suggesting that the source is in the faint, intermediate state (D in Fig. 1) consistent with the non-detection in the radio. The SWIFT XRT and BAT results suggest a sharp turn over in flux at high energies.

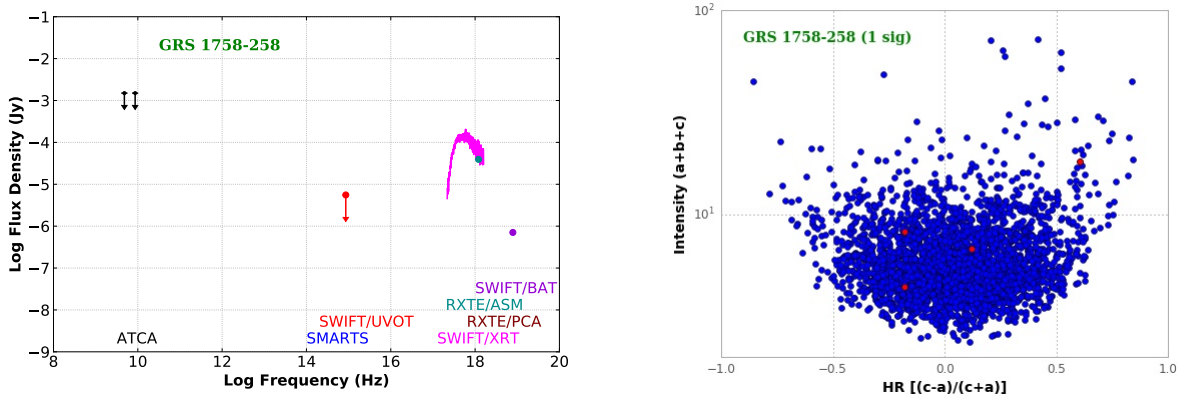


Figure 12. Spectral Energy Distribution and color-intensity plots of GRS 1758-258. The panels and axes are as in figure 11.

GRS 1758-258 (Fig. 12; Fig. 32.13.) is a persistent, low-flux source. It is known to have a clear connection between the radio jet and the ISM (Tetarenko et al. 2020). However, during the campaign there are only upper limits from the ATCA and Swift UVOT. There are consistent flux densities measured by the Swift XRT and RXTE ASM. It is unclear if the BAT result is high or low: it depends on how the spectrum turns over. The RXTE PCA CI diagram in addition to the non-detection in the radio is consistent with the source being in the intermediate low state (D in Fig. 1).

GRS1915+105 (V1487 Aql, Fig. 13; Fig. 32.33) is a continuously active but variable source. It was not observed with the ATCA. It is detected at K-band with SMARTS; the IR flux is likely dominated by the companion star. It was not observed by the Swift XRT. In the ASM data it ranges from 10-170 cts s⁻¹. The week of this campaign it was on a steeply rising slope at 80 cts s⁻¹. The ASM flux falls below the RXTE PCA spectrum; the ASM is averaged over the week and the PCA observation was taken later in the week so the two are consistent. The BAT measurement is consistent with the RXTE PCA. The PCA gives the highest flux of all the BHs. During the week of this campaign

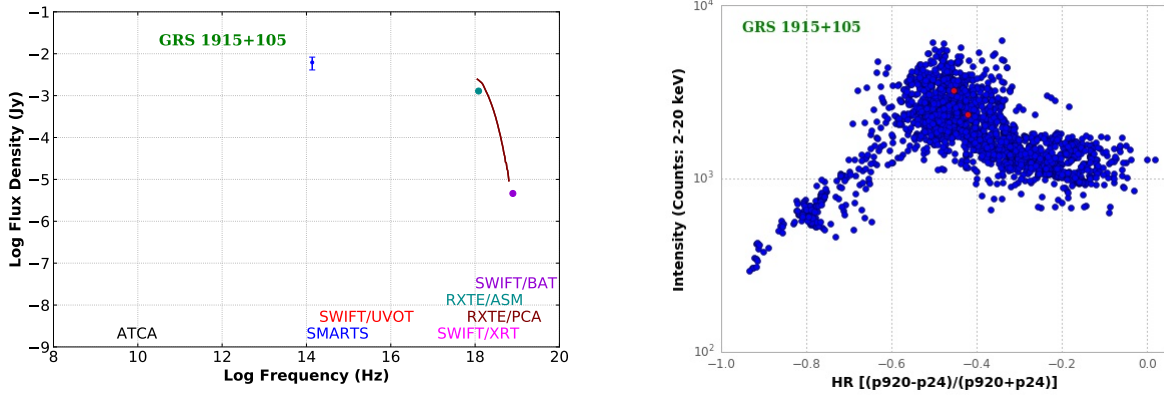


Figure 13. Spectral Energy Distribution and color-intensity plots of GRS 1915+105. The panels and axes are as in figure 9.

GRS1915+105 was in the Bright/Intermediate state based on the RXTE PCA CI diagram (B in Fig. 1. A resolved radio jet is expected in this state (Arur and Maccarone 2022).

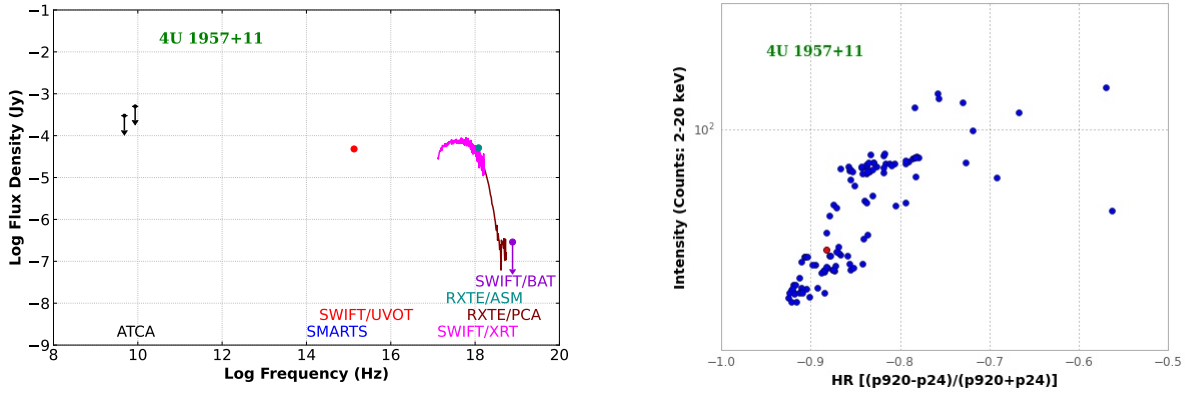


Figure 14. Spectral Energy Distribution and color-intensity plots of 4U 1957+11. The panels and axes are as in figure 9.

4U 1957+11 (V1408 Aql, Fig. 14; Fig. 32.16.) is a continuously active variable source. It is one of the fastest spinning BHs (Nowak et al. 2011). It shows upper limits with the ATCA. The SWIFT/XRT and BAT and the RXTE/PCA and ASM all give consistent flux densities. The PCA CI plot together with the non detection in the radios implies that it is in the A2 state (Fig. 1) when the radio jet is quenched.

3.1.1. X-ray Non-Detections (BHs: 5)

Many of our sources have detections in the infrared, optical, and/or ultraviolet only, but no detection or minimal data in the X-rays. These are generally X-ray transients in quiescence, and only the companion star is visible in this phase. They all show upper limits from the ATCA, consistent with radio flux at the μJy level. These include LMC X-1 (4U 0540-697), XTE J1550-564 (V381 Nor), 4U 1630-47, GRO J1655-40, and V4641 Sgr.

3.2. Z sources (8 sources; 5 with SEDs)

Cir X-1 (4U 1516-56; BR Cir, Fig. 15; Fig. 32.32.) is a highly variable source ranging from 0-200 ASM cts s^{-1} . During the week of this campaign it was below the detection limit of the ASM. There are positive detections with the ATCA and SMARTS, upper limits with the Swift UVOT. The XRT spectrum shows a dip at 5.5×10^{17} Hz that is apparent during very low X-ray flux (Schulz et al. 2020). While a single blackbody with very small area has been fit at this state (Schulz et al. 2020), the XRT found a blackbody temperature to be unconstrained (25 ± 100 keV). There

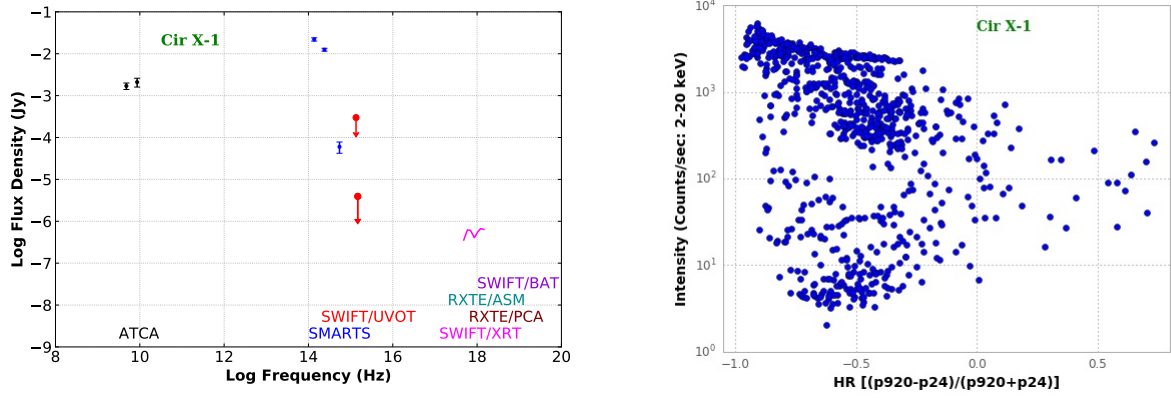


Figure 15. Spectral Energy Distribution and color-intensity plots of Cir X-1. The X-ray spectrum is from Obsid 00030268025 on Table 6 (SWIFT/XRT). The panels and axes are as in figure 9.

is no significant detection by the Swift BAT during the week of the campaign. It was not observed by the RXTE PCA during the week of the campaign.

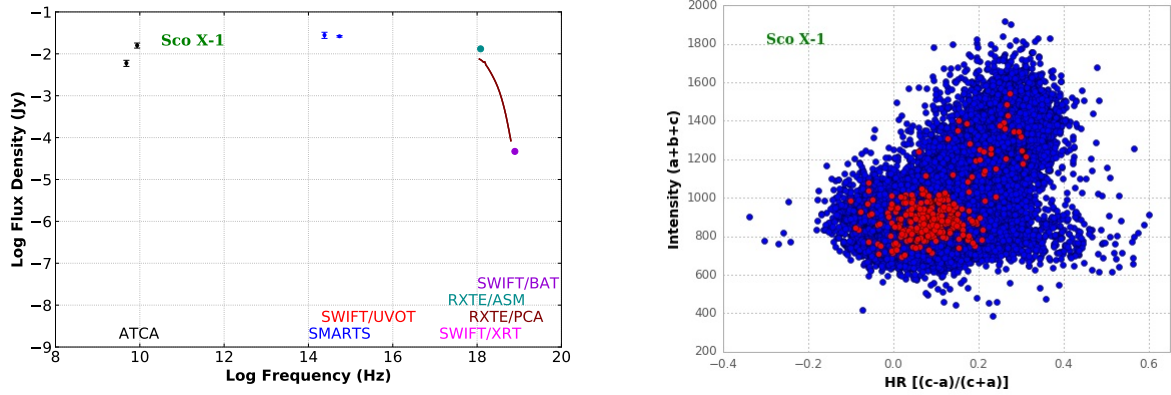


Figure 16. Spectral Energy Distribution and color-intensity plots of Sco X-1. The panels and axes are as in figure 11.

Sco X-1 (4U 1617-15; V818 Sco, Fig. 16; Fig. 32.40.) is a very bright, persistent source. We have positive detections with ATCA at the mJy level, and a positive detection with SMARTS. The flux density values are consistent between the RXTE PCA, and the Swift BAT; the flux density is slightly high in the RXTE ASM. The ASM CI plot, using dwell by dwell values (6-8 per day), shows that while Sco X-1 is mostly in the NB there are several excursions into FB. This explains the discrepancy between the ASM and PCA spectra. The lightcurves plotted with one day averages do not resolve the flares. This source has the highest radio flux density of all the sources in this campaign. The rapidly variation seen by the ATCA is consistent with the emergence of a jet as expected for this source in the NB.

XTE J1701-462 (Fig. 17; Fig. 32.37.) is a transient source on a downward trend of a strong outburst. It shows upper limits with the ATCA. SMARTS has positive detections at all frequencies. The flux density measured with the Swift XRT is high. The PCA data matches the ASM and BAT results. As a source that shows both Z and Atoll behavior, it appears to be at a transition between the two based on the RXTE PCA CI plots. The lack of a radio detection, consistent with no jet, would be consistent with the flaring (Z) branch (Homan et al. 2010).

GX 349+2 (4U 1702-36; V1101 Sco, Fig. 18; Fig. 32.21.) is a bright persistent source that has frequent flares (Coughenour et al. 2018). The ATCA gives flux density upper limits. SMARTS has positive detections. The Swift UVOT has one upper limit. The Swift XRT flux density is low compared with the RXTE PCA, which matches the RXTE ASM and Swift BAT results. During the week of the campaign GX 349+2 was in the cusp between FB and

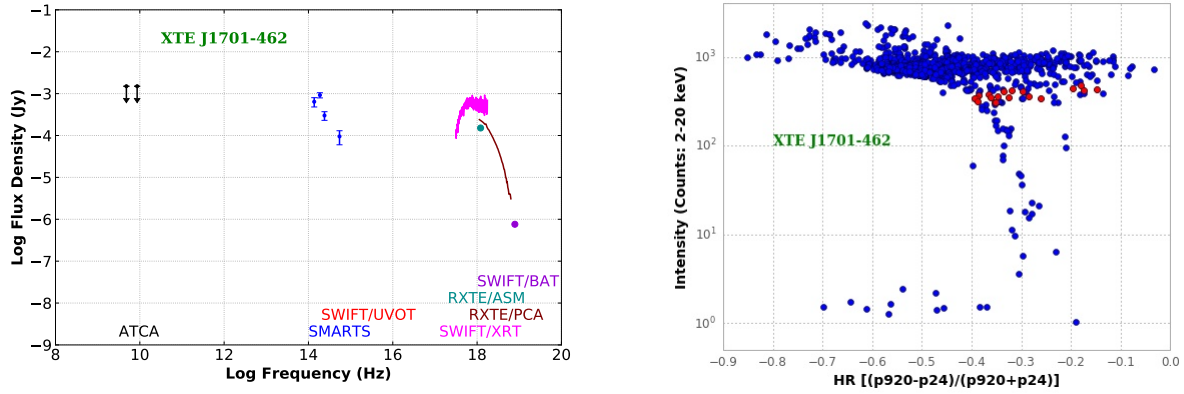


Figure 17. Spectral Energy Distribution and color-intensity plots of XTE J1701-462. The panels and axes are as in figure 9.

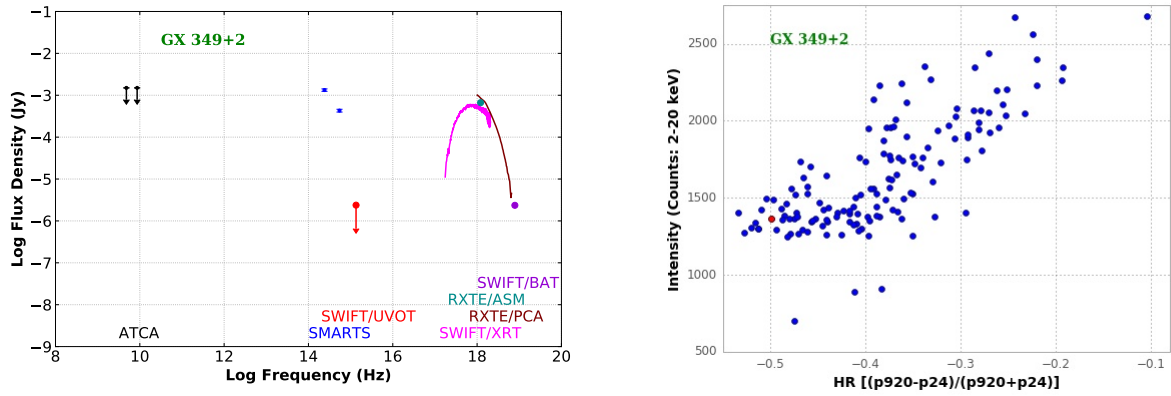


Figure 18. Spectral Energy Distribution and color-intensity plots of GX 349+2. The panels and axes are as in figure 9.

NB based on the RXTE PCA CI diagram. The upper limit in radio favors the FB where the radio is quenched. The flux discrepancy between XRT and PCA suggests the PCA caught a flare.

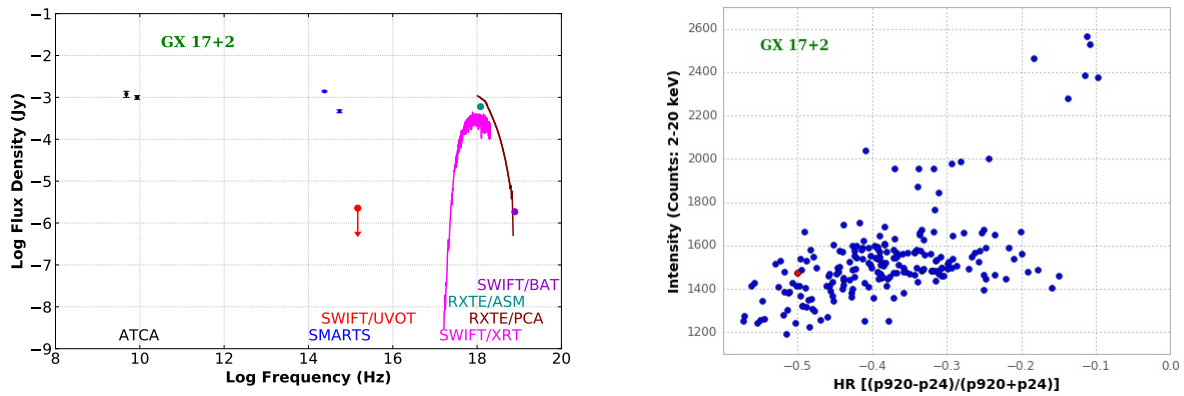


Figure 19. Spectral Energy Distribution and color-intensity plots of GX 17+2. The X-ray spectrum plots both Obsids 00035340006 and 00035340007 on Table 6 (SWIFT/XRT). The panels and axes are as in figure 9.

GX 17+2 (4U 1813-14; NP Ser, Fig. 19; Fig. 32.18.) is a bright persistent steady source. It shows a detection by the ATCA at the mJy level, and detections by SMARTS. It shows an upper limit with the Swift UVOT. In the campaign week it was in the cusp between FB and NB state based on the RXTE PCA CI diagram; the presence of radio emission suggests a jet and hence the NB state.

3.2.1. X-ray Non-Detections (Z-sources: 3)

LMC X-2, GX 340+0, and GX 5-1 were not detected in either the RXTE-PCA or the SWIFT-XRT.

3.3. Atoll Sources (18 sources; 9 with SEDs)

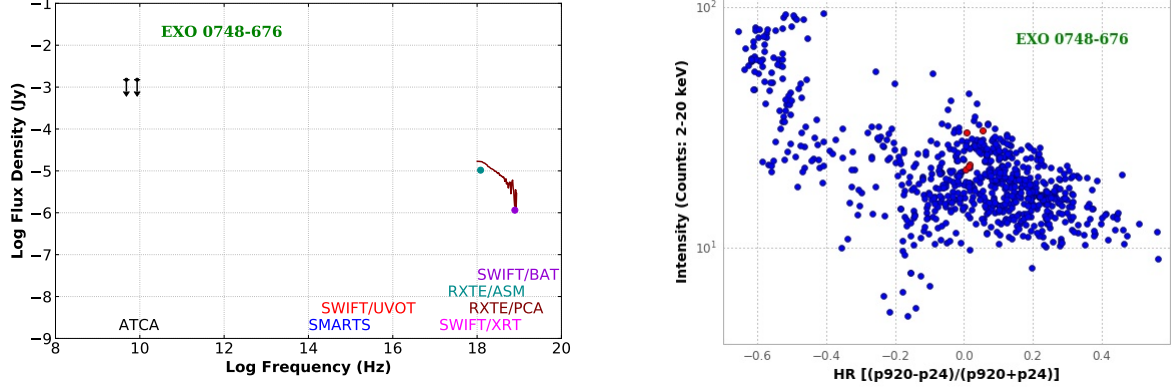


Figure 20. Spectral Energy Distribution and color-intensity plots of EXO 0748-676. The panels and axes are as in figure 9.

EXO 0748-67 (UY Vol, Fig. 20; Fig. 32.2.) is a burster. It is mostly at the level of 1 ASM cts s⁻¹, with bursts up to 4 ASM cts s⁻¹. During the campaign week it was at the 1 ASM cts s⁻¹ level. The ATCA gives upper limits. The RXTE PCA flux density is consistent with the Swift BAT upper limit. The RXTE ASM flux density is slightly low. In the campaign week it was in the LB state based on the RXTE PCA CI diagram.

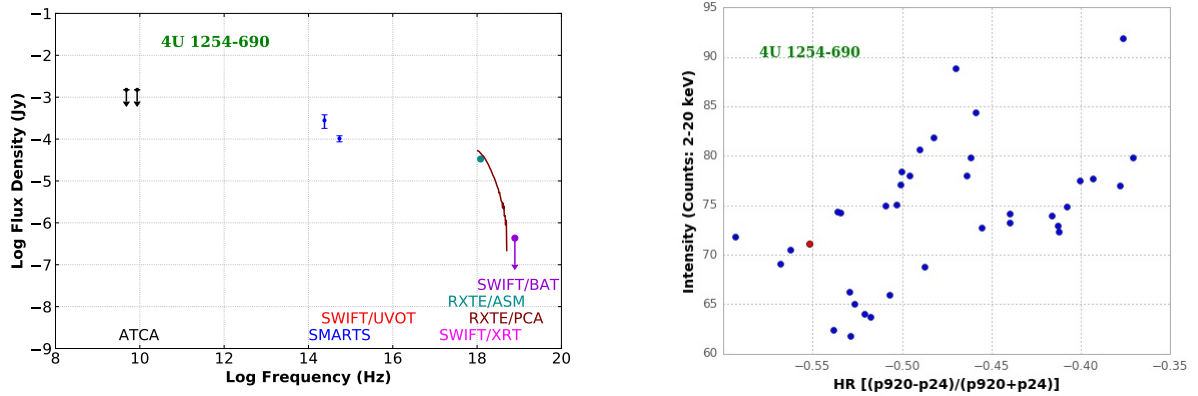


Figure 21. Spectral Energy Distribution and color-intensity plots of 4U 1254-690. The panels and axes are as in figure 9.

4U 1254-69 (GR Mus, Fig. 21; Fig. 32.3.) is a burster with source persistent at about 3 ASM cts s⁻¹. It is one of four bursters that have shown a superburst in connection with the regular burst (in't Zand et al. 2003). The ATCA gives upper limits. SMARTS gives one upper limit and one detection. The RXTE PCA is consistent with the RXTE ASM. The Swift BAT gives an upper limit. During the campaign week it was on the cusp between the LB and the UB state based on the RXTE PCA CI diagram.

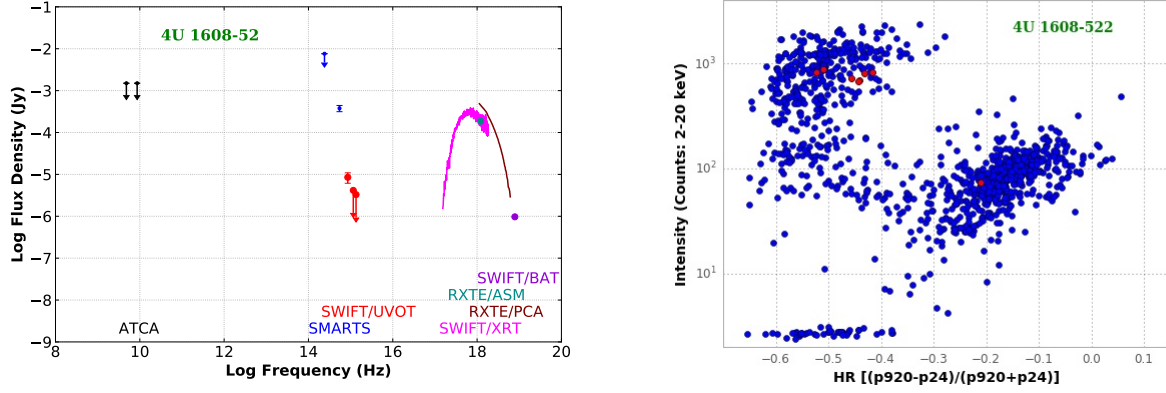


Figure 22. Spectral Energy Distribution and color-intensity plots of 4U 1608-52. The X-ray spectrum plots the average of three Obsids on Table 10 (RXTE/PCA) and Obsid 00030791018 on Table 6 (SWIFT/XRT). The panels and axes are as in figure 9.

4U 1608-522 (QX Nor, Fig. 22; Fig. 32.5.) is a transient burster. Most of the time it is not detected by the ASM, but accretion disk outbursts reach up to 65 cts s^{-1} . During our campaign week it was at the downturn of an outburst at 20 ASM cts s^{-1} . This is consistent with it being in the propeller state (Asai et al. 2013; Matsuoka and Asai 2013). The derived value of N_H varies by more than the error bars on Table 6, col. 8, after MJD 54284. If this variation is real, it may be linked to the pile-up of accretion disk material expected during the onset of the propeller phase (e.g. Lii et al. 2014). The PCA data matches the BAT data, but it gives a higher flux density than the ASM and XRT. Its status during our campaign week is consistent with the UB state based on the RXTE PCA CI diagram.

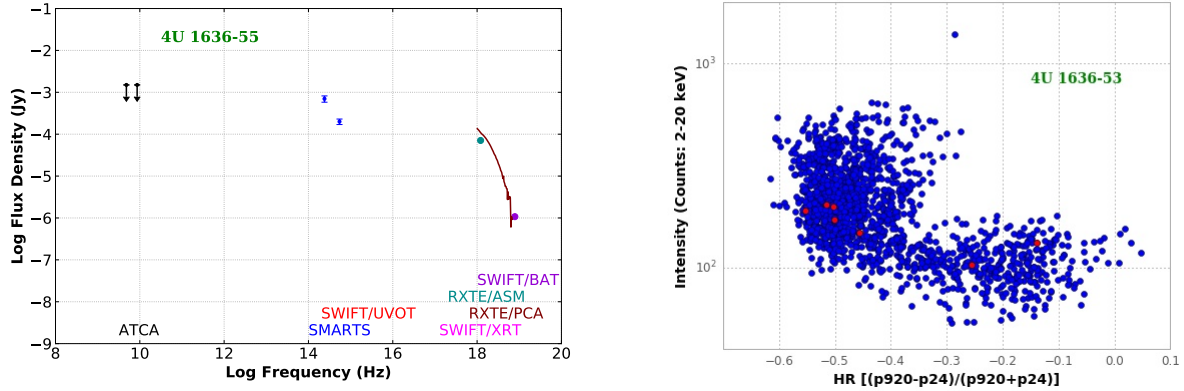


Figure 23. Spectral Energy Distribution and color-intensity plots of 4U 1636-53. The panels and axes as in figure 9.

4U 1636-53 (V801 ArA, Fig. 23; Fig. 32.6.) is a persistent but variable source, with maxima reaching up to 20 ASM cts s^{-1} lasting from 10-20 days. It is one of four bursters that have shown a superburst in connection with the regular burst (in't Zand et al. 2003; Strohmayer and Markwardt 2002). Our campaign week was during the downside of an outburst (10 cts s^{-1}). The ATCA shows upper limits. SMARTS has positive detections. The RXTE PCA result matches those of the RXTE ASM and Swift BAT. During the campaign week it was in the cusp between LB and UB and it shows excursions into the LB state based on the RXTE PCA CI diagram.

4U 1705-44 (Fig. 24; Fig. 32.10.) is a persistent but variable source, with maxima reaching up to 30 ASM cts s^{-1} lasting from 20-40 days (Phillipson et al. 2018). During the campaign week it was on the downside of an outburst (15 cts s^{-1}). The ATCA gives an upper limit. The RXTE PCA flux density matches the RXTE ASM and Swift BAT results. In the campaign week it was in the UB state based on the RXTE PCA CI diagram.

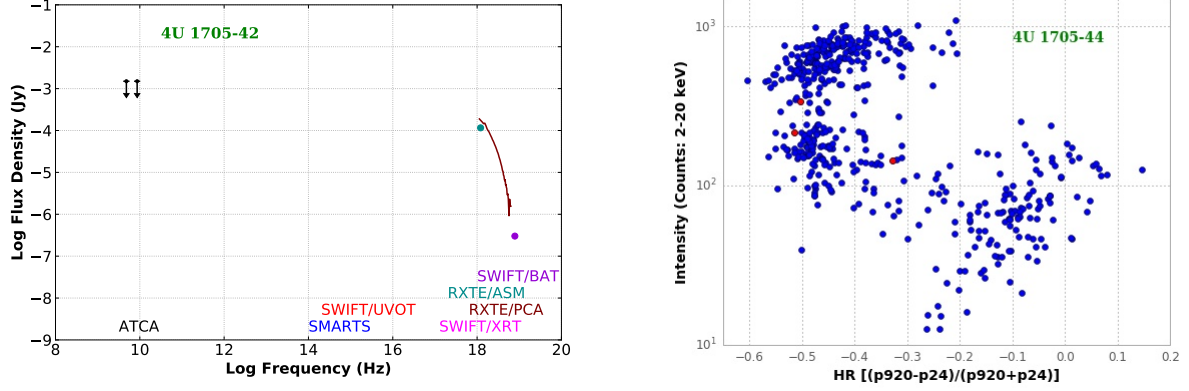


Figure 24. Spectral Energy Distribution and color-intensity plots of 4U 1705-44. The X-ray spectrum plots the average of the two observations on Table 10 (RXTE/PCA). The panels and axes as in figure 9.

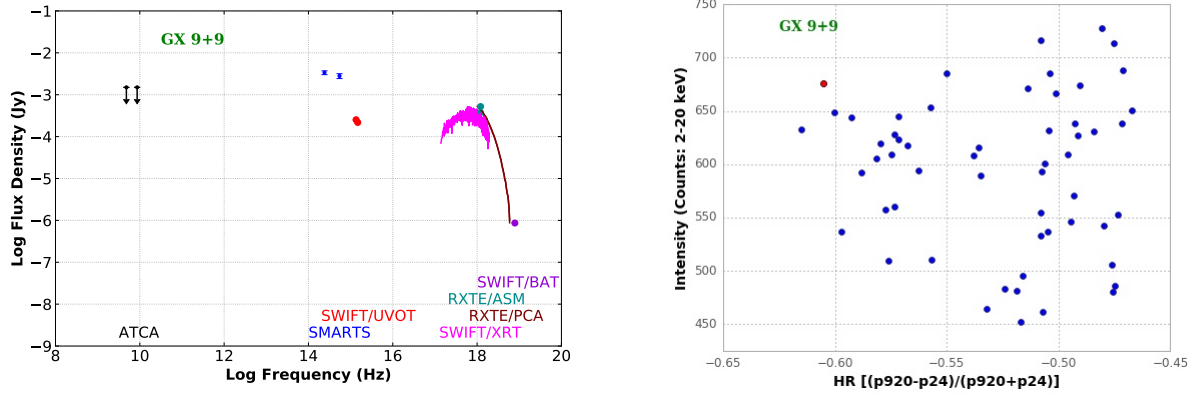


Figure 25. Spectral Energy Distribution and color-intensity plots of GX 9+9. The X-ray spectrum plots all three Obsids on Table 6 (SWIFT/XRT). The panels and axes as in figure 9.

GX 9+9 (4U 1728-16; V2216 Oph, Fig. 25; Fig. 32.37.) is a bright, persistent, smoothly varying source, typically giving 15 to 25 ASM cts s⁻¹; during our campaign it was at a level of 25 cts s⁻¹. The ATCA gives upper limits; SMARTS and the UVOT give positive detections. Flux densities from the Swift XRT, RXTE PCA, ASM, and BAT are all consistent. During the campaign week it was in the UB state based on the RXTE PCA CI diagram.

GX 354+0 (4U 1728-337, Fig. 26; Fig. 32.22.) is a persistent burster. It typically ranges from 5-20 ASM cts s⁻¹. During our week it was at 7 cts s⁻¹. It is unusual for an Atoll source in that radio detections consistent with a jet have been reported (Migliari et al 2003). The ATCA and Swift UVOT give upper limits. The Swift XRT flux density is consistent with the RXTE ASM. It is unclear if the BAT is high or low: that depends on how the spectrum turns over. During our campaign week it was in the IS based on the RXTE PCA CI diagram.

4U 1735-44 (V926 Sco, Fig. 27; Fig. 32.11.) is a bright, persistent, smoothly varying source; it typically ranges from 5 to 30 ASM cts s⁻¹. During our week it was between 12 and 15 cts s⁻¹. The ATCA gives upper limits. SMARTS and the Swift UVOT give positive detections. Results from the RXTE PCA, RXTE ASM, Swift XRT, and Swift BAT all match. It was in UB and IS based on the RXTE PCA CI diagram.

Aql X-1 (4U 1908+00, Fig. 28; Fig. 32.22.) is a transient burster; it ranges from 0-50 ASM cts s⁻¹ec. It was not observed by the ATCA. It shows positive detections with SMARTS and the Swift UVOT. Flux densities from the Swift XRT and RXTE PCA are consistent. There was no significant detection with the RXTE ASM during the week of the campaign, however the lightcurve shows that it was caught shortly after a small outburst. It was in the LB state based on the RXTE PCA CI diagram.

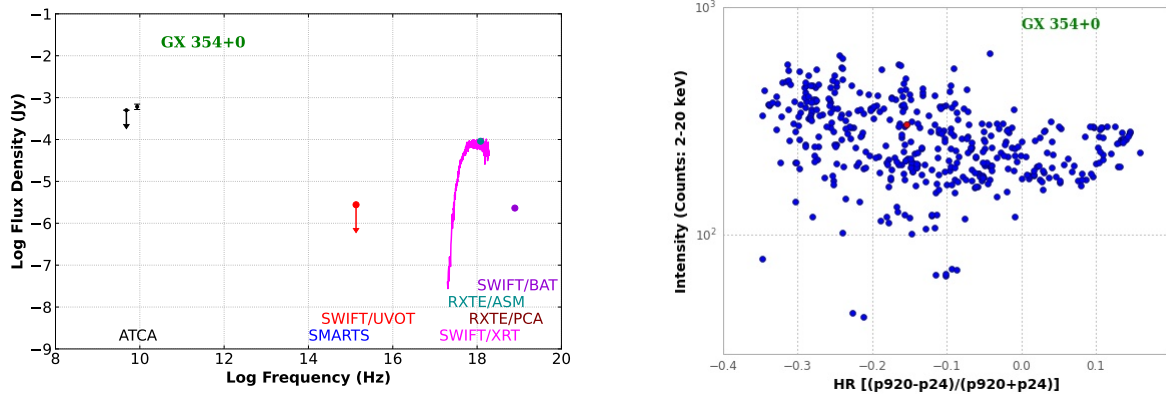


Figure 26. Spectral Energy Distribution and color-intensity plots of GX 354+0. The panels and axes as in figure 9.

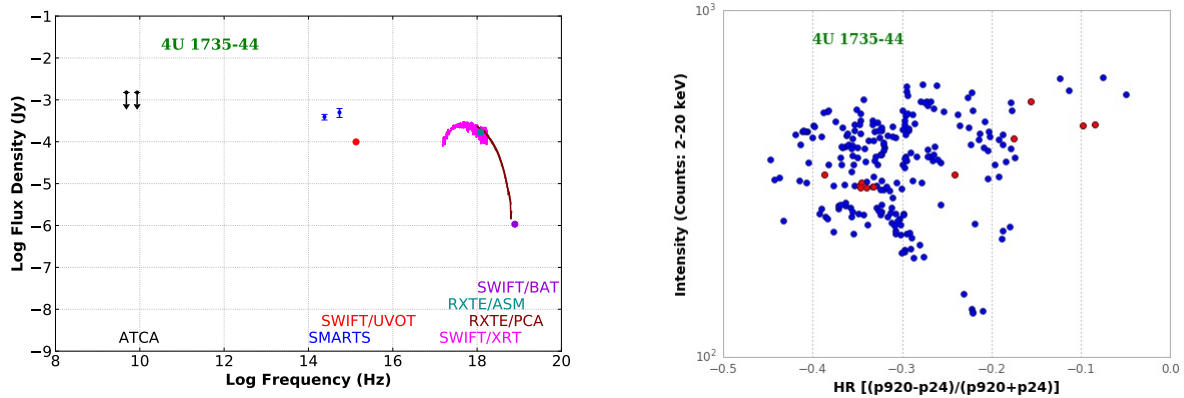


Figure 27. Spectral Energy Distribution and color-intensity plots of 4U 1735-44. The panels and axes as in figure 9.

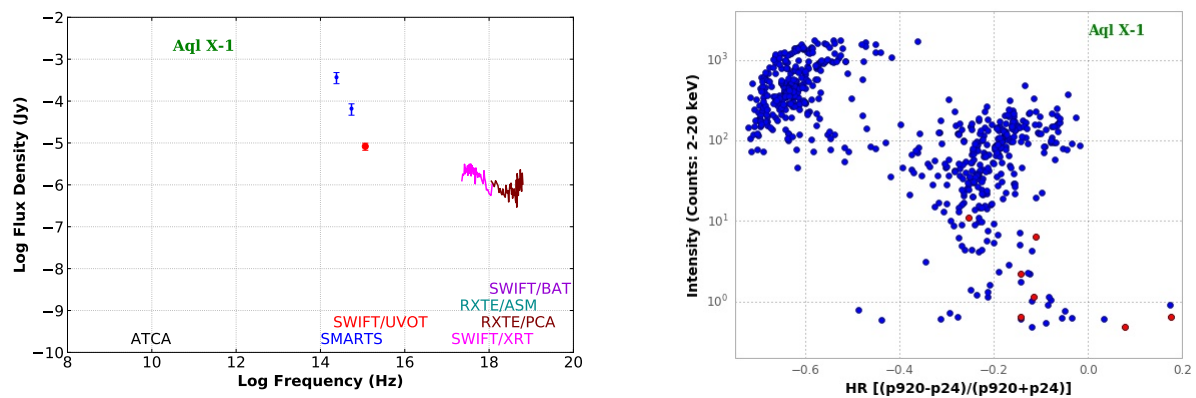


Figure 28. Spectral Energy Distribution and color-intensity plots of Aql X-1. The X-ray spectrum plots Obsid 30796022 on Table 6 (SWIFT/XRT). The panels and axes as in figure 9.

3.3.1. X-ray Non-Detections (Atolls: 9)

2S 0921-630 (V395 Car) and Cen X-4 (4U 1456-32; V822 Cen) give only upper limits with the ATCA and the RXTE ASM. Cen X-4 is an SXT and a burster. It gives positive detections in SMARTS. 4U 1543-624 (QU TrA), 4U 1556-60

(LU TrA), MXB 1658-298 (4U 1704-30, V2134 Oph), 4U 1702-429 (Ara X-1), GX 3+1 (4U 1744-26, Sgr X-1), GX 9+1 (4U 1758-20, Sgr X-3), and GX13+1 (Sgr X-2, V5512 Sgr) also show radio non-detections and minimal X-ray data.

3.4. Pulsars (11 sources; 3 with sed)

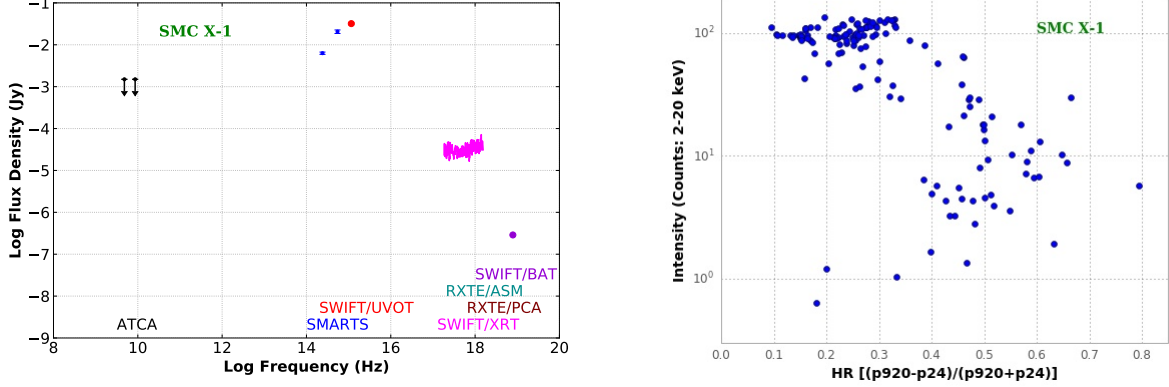


Figure 29. Spectral Energy Distributions and color-intensity plots of SMC X-1. The panels and axes as in figure 9.

SMC X-1 (4U 0115-73; SK 160, Fig. 29; Fig. 32.41.) is a pulsar with a superorbital period varying from 40-60 days (Pradhan et al. 2020). There is some evidence of a correlation between spin and superorbital periods (Hu et al. 2023). During the week of the campaign it was in the uprise of the superorbital period. It gives upper limits with the ATCA, and detections in SMARTS, the UVOT, and the SWIFT XRT and BAT. Its SED is very similar to that of 4U 1822-371 (Fig. 30).

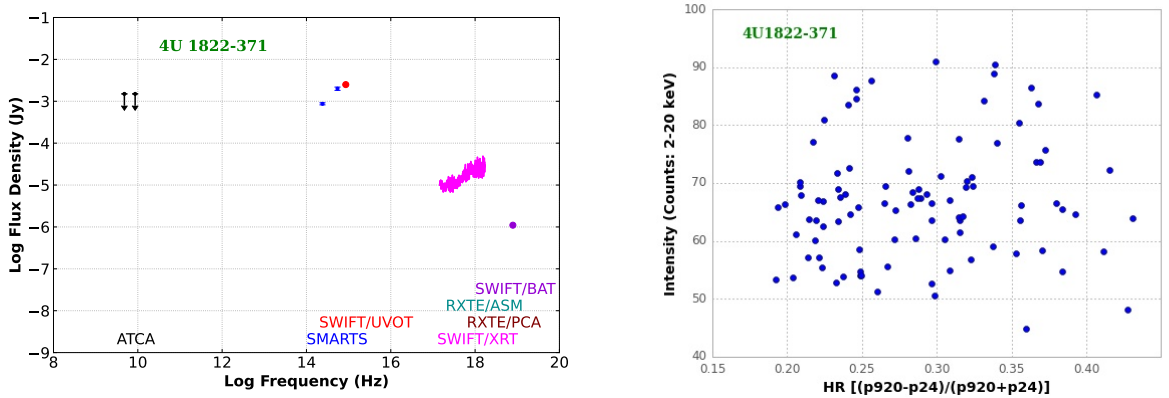


Figure 30. Spectral Energy Distribution and color-intensity plots of 4U 1822-371. The panels and axes as in figure 9.

4U 1822-371 (V691 CrA, Fig. 30; Fig. 32.14.) is one of the few low mass XRBs to show pulsations. During the campaign week it was below the detection limit of the ASM and PCA. It shows upper limits with the ATCA, there are positive detections with SMARTS, the UVOT, the SWIFT XRT and the SWIFT BAT. The SEDs for SMC X-1 (Fig. 29) and 4U 1822-371 are remarkably similar, both showing rising spectra near 10 Hz (4 keV) with the SWIFT XRT, but a rapid drop in flux density at the higher energies of the BAT (30 keV).

4U 1907+09 (Fig. 31; Fig. 32.28.) is relatively weak in X-rays. It was not observed with the ATCA. It shows positive detections in SMARTS. There is no significant detection by the RXTE ASM during the week of the campaign. The Swift XRT shows a sharp drop off consistent with the Swift BAT detection. It covers the full area typical for pulsars in the RXTE PCA CI diagram.

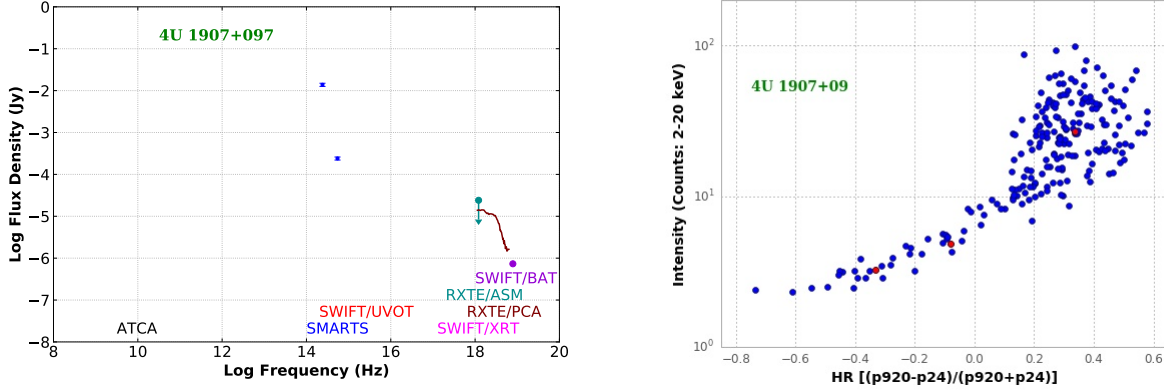


Figure 31. Spectral Energy Distribution and color-intensity plots of 4U 1907+097. The X-ray spectrum plots the observation at MJD 54282.398 on Table 10 (RXTE/PCA). The panels and axes as in figure 9.

3.4.1. X-ray Non-Detections (8)

SMC X-3 (Lin 198), GX 1+4 (4U 1728-24, V2216 Oph (sometimes classed as a symbiotic star), and Swift J1756.9-2508, show only upper limits in the radio and X-rays. SMC X-1 (4U 0115-73, SK 160) Vela X-1 (4U 0900-40, GP Vel), Cen X-3 (4U 1119-603, V779 Cen), GX 301-2 (4U 1223-62, BP Cru), 4U 1538-522 (QV Nor), and 4U 1700-37 (HD 153919) all show only upper limits in the radio and have little or no X-ray data.

4. CONCLUSIONS

Multi-wavelength observations of black hole and neutron star XRBs show trends that demonstrate important connections between the accretion disk, the nature of the compact object and jet production. Jet theories invoke a poloidal magnetic field configuration arising from the accretion disk that collimates the jet flow (Ferreira 2008). Fender et al. (2004) use magnetic field strengths to rank XRBs from most likely to least likely to produce jets: BHs, Z-types, Atoll-types, and Pulsars. Massi & Kaufman Bernadó (2008) quantify this progression noting that high magnetic fields hinder the production of jets and high accretion rates enhance the production of jets. Our observations are consistent with these interpretations: we detect no significant radio emission from pulsars or atolls, but we do detect radio emission from Z sources in the normal or horizontal branch, and from BHs in the soft/high, hard/low and quiescent states.

Ten out of 11 BH systems were observed by the ATCA, four of these (LMC X-3, GX 339-4, 1E 1740.7-2942, and GRS 1758-258) have simultaneous X-ray spectra from Swift/XRT and/or RXTE/PCA. LMC X-3 is in the faint intermediate state with radio upper limits consistent with no jet; LMC X-1 is in the intermediate/low state (inferred from the RXTE/ASM CI) with upper limits in radio emission consistent with no jet; GX 339-4 is in a hard/low state with radio flux of a few mJy consistent with a continuously active, flat-spectrum, compact, resolved jet; 1E 1740.7-2942 is relatively faint, with a radio flux upper limit consistent with a μ Jy level compact radio jet; GRS 1758-258 is in a faint intermediate state with radio upper limits consistent with no jet; XTE J1550-564, 4U 1630-47, and GRO J1655-40 are all below the detection limit in the ASM with undetected radio flux, consistent with the expected levels at quiescence. V4641 Sgr was not observed in X-rays; GRS 1915+105 is in the bright/intermediate state but was not observed in the radio. 4U 1957+11 is in the soft/low state with upper limits from the ATCA consistent with no jet.

Five of eight Z sources observed by the ATCA have simultaneous X-ray spectra from Swift XRT and/or RXTE PCA (Cir X-1, Sco X-1, XTE J1701-462, GX 349+2, and GX 17+2); for the other three (LMC X-2, GX 340+0, and GX 5-1) we are able to infer the X-ray state from the RXTE ASM data. LMC X-2 is in a mini-flare with only upper limits from the ATCA consistent with no radio emission; Cir X-1 is a peculiar source, at very low X-ray luminosity with radio emission at the mJy level consistent with the HB, but no RXTE ASM detection during the week of the campaign. Sco X-1, known to be a resolved jet source, was mostly in the NB with excursions into FB, having radio emission of tens of mJy consistent with the presence of a jet. GX 340+0, GX 5-1, and GX 17+2 are all in the NB of the Z and have radio detections at the mJy level consistent with a transient jet; J1701-462 is a transient source in outburst, with upper limits from the ATCA. The HB state inferred from the RXTE PCA CI is consistent with no jets at this X-ray state.

The 18 Atoll sources yielded only upper limits from the ATCA. This is consistent with Atoll sources having at most an unresolved radio source with flux density at the microJy level. Of nine pulsars none were detected by the ATCA, consistent with expectations.

We are grateful to Alberto Pasten for running the observations at CTIO.

The Australia Telescope Compact Array is part of the Australia Telescope National Facility which is funded by the Australian Government for operation as a National Facility managed by CSIRO.

This publication makes use of data products from the Two Micron All Sky Survey, which is a joint project of the University of Massachusetts and the Infrared Processing and Analysis Center/California Institute of Technology, funded by the National Aeronautics and Space Administration and the National Science Foundation. This research also used data from the AAVSO Photometric All Sky Survey (APASS) DR9 (Henden et al. 2015). This research has also made use of NASA’s Astrophysics Data System as well as the VizieR catalogue access tool, Centre de Donn’ees astronomiques de Strasbourg, Strasbourg, France.

The authors are grateful to an anonymous referee for helpful criticism and suggestions.

Software: This research made use of SciPy (Virtanen et al. 2020), NumPy (van der Walt et al. 2011), Matplotlib, a Python library for publication quality graphics (Hunter 2007), Astropy (<http://www.astropy.org>), a community-developed core Python package for Astronomy (Astropy Collaboration et al. 2013), MIRIAD (Sault, Teuben & Wright 1995), HEASoft (HEASARC 2014), KARMA (Gooch 1996), and XSPEC (Arnaud 1996).

Facilities: Australia Telescope Compact Array (ATCA), Two Micron All Sky Survey (2MASS), Small and Moderate Aperture Research Telescope System (SMARTS), Swift Burst Alert Telescope (BAT), Swift Ultraviolet and Optical Telescope (UVOT), Swift X-Ray Telescope (XRT), RXTE All Sky Monitor (ASM), Rossi X-ray Timing Explorer Proportional Counter Array (RXTE-PCA)

REFERENCES

- Arnaud, K.A., 1996, *Astronomical Data Analysis Software and Systems V*, A.S.P. Conference Series, Vol. 101, George H. Jacoby and Jeannette Barnes, eds., p. 17.
- Arur, K., and Maccarone, T.J., 2022, *MNRAS*, 514, 1720.
- Asai, K., Matsuoka, M., Mihara, T., et al. 2013, *ApJ*, 773, 117A.
- Astropy Collaboration, Robitaille, T. P., Tollerud, E. J., et al. 2013, *A&A*, 558, A33, doi: [10.1051/0004-6361/201322068](https://doi.org/10.1051/0004-6361/201322068)
- Bailer-Jones, C. A. L., Rybizki, J., Fouesneau, M., Demleitner, M., & Andrae, R. 2021, *VizieR Online Data Catalog*, I/352
- Balucinska-Church, M., Gibiec, A., Jackson, N.K., and Church, M.J., 2010, *A&A*512, A9.
- Barthelmy, S. D., Barbier, L. M., Cummings, J. R., et al. 2005, *SSRv*, 120, 143, doi: [10.1007/s11214-005-5096-3](https://doi.org/10.1007/s11214-005-5096-3)
- Belloni, T., Homan, J., Casella, P., et al. 2005, *A&A*, 440, 207, doi: [10.1051/0004-6361:20042457](https://doi.org/10.1051/0004-6361:20042457)
- Bhuvana, G.R., Radhika, D., Agrawal, V.K., Mandal, S., and Nandi, A., 2021, *MNRAS*, 501, 5457.
- Burrows, D. N., Hill, J. E., Nousek, J. A., et al. 2005, *SSRv*, 120, 165, doi: [10.1007/s11214-005-5097-2](https://doi.org/10.1007/s11214-005-5097-2)
- Church, M.J., Gibiec, A., Balucinska-Church, M., Jackson, N.K., 2012, *A&A*546, 35C.
- Cohen, M., Wheaton, W. A., & Megeath, S. T. 2003, *AJ*, 126, 1090, doi: [10.1086/376474](https://doi.org/10.1086/376474)
- Cox, A. N. 2000, *Allen’s astrophysical quantities* (New York: AIP Press; Springer)
- Cutri, R. M., Skrutskie, M. F., van Dyk, S., et al. 2003, *VizieR Online Data Catalog*, II/246
- de Beurs, Z. L., Islam, N., Gopalan, G., & Vrtilek, S. D. 2022, *arXiv e-prints*, arXiv:2204.00346. <https://arxiv.org/abs/2204.00346>
- Dickey, J. M., Weston, J. H. S., Sokoloski, J. L., Vrtilek, S. D., & McCollough, M. 2021, *ApJ*, 911, 30, doi: [10.3847/1538-4357/abe774](https://doi.org/10.3847/1538-4357/abe774)
- Fender, R., Corbel, S., Tzioumis, T., et al. 1999, *ApJL*, 519, L165, doi: [10.1086/312128](https://doi.org/10.1086/312128)
- Fender, R. P., Belloni, T. M., & Gallo, E. 2004, *MNRAS*, 355, 1105, doi: [10.1111/j.1365-2966.2004.08384.x](https://doi.org/10.1111/j.1365-2966.2004.08384.x)
- Ferreira, J. 2008, *NewAR*, 52, 42, doi: [10.1016/j.newar.2008.04.003](https://doi.org/10.1016/j.newar.2008.04.003)
- Fomalont, E. B., Geldzahler, B. J., & Bradshaw, C. F. 2001, *ApJ*, 558, 283, doi: [10.1086/322479](https://doi.org/10.1086/322479)
- Gaia Collaboration, Brown, A. G. A., Vallenari, A., et al. 2018, *A&A*, 616, A1, doi: [10.1051/0004-6361/201833051](https://doi.org/10.1051/0004-6361/201833051)
- Gallo, E., Degenaar, N., & van den Eijnden, J. 2018, *MNRAS*, 478, L132, doi: [10.1093/mnrasl/sly083](https://doi.org/10.1093/mnrasl/sly083)

- Gallo, L. C., Wilkins, D. R., Bonson, K., et al. 2015, MNRAS, 446, 633, doi: [10.1093/mnras/stu2108](https://doi.org/10.1093/mnras/stu2108)
- Garcia, M. R., McClintock, J. E., Narayan, R., et al. 2001, ApJL, 553, L47, doi: [10.1086/320494](https://doi.org/10.1086/320494)
- Gehrels, N., Chincarini, G., Giommi, P., et al. 2004, ApJ, 611, 1005, doi: [10.1086/422091](https://doi.org/10.1086/422091)
- Gooch, R. 1996, in Astronomical Society of the Pacific Conference Series, Vol. 101, Astronomical Data Analysis Software and Systems V, ed. G. H. Jacoby & J. Barnes, 80
- Gopalan, G., Vrtillek, S. D., & Bornn, L. 2015, ApJ, 809, 40, doi: [10.1088/0004-637X/809/1/40](https://doi.org/10.1088/0004-637X/809/1/40)
- Guillot, S., Kerr, M., Ray, P.S., et al., 2019, ApJL, 887, L27.
- Hasinger, G., & van der Klis, M. 1989, A&A, 225, 79
- High Energy Astrophysics Science Archive Research Center (Heasarc), 2014, Astrophysics Source Code Library, record ascl:1408.004.
- Henden, A.A., Levine, S., Terrell, D., and Welch, D.L., 2015, American Astronomical Society, AAS Meeting 225, id.336.16
- HI4PI Collaboration, Ben Bekhti, N., Flöer, L., Keller, R. et al., 2016, A&A, 594, id.A116.
- Homan, J., van der Klis, M., Fridriksson, J. K., et al. 2010, ApJ, 719, 201, doi: [10.1088/0004-637X/719/1/201](https://doi.org/10.1088/0004-637X/719/1/201)
- Hu, C-P., Dage, K.C., Clarkson, W.I., et al., 2023, MNRAS, 520, 3436H.
- Hunter, J. D. 2007, Computing in Science and Engineering, 9, 90, doi: [10.1109/MCSE.2007.55](https://doi.org/10.1109/MCSE.2007.55)
- Kalemci, E., Tomsick, J. A., Buxton, M. M., et al. 2005, ApJ, 622, 508, doi: [10.1086/427818](https://doi.org/10.1086/427818)
- Levine, A. M., Bradt, H., Cui, W., et al. 1996, ApJL, 469, L33, doi: [10.1086/310260](https://doi.org/10.1086/310260)
- Lii, P.S., Romanova, M.M., Ustyugova, G.V., et al., 2014, MNRAS, 441, 86.
- Liu, Q. Z., van Paradijs, J., & van den Heuvel, E. P. J. 2001, A&A, 368, 1021, doi: [10.1051/0004-6361:20010075](https://doi.org/10.1051/0004-6361:20010075)
- . 2006, A&A, 455, 1165, doi: [10.1051/0004-6361:20064987](https://doi.org/10.1051/0004-6361:20064987)
- Massi, M., & Kaufman Bernadó, M. 2008, A&A, 477, 1, doi: [10.1051/0004-6361:20077567](https://doi.org/10.1051/0004-6361:20077567)
- Matsuoka, M. and Asai, K., 2013, PASJ, 65, id.26.
- McClintock, J. E., Haswell, C. A., Garcia, M. R., et al. 2001, ApJ, 555, 477, doi: [10.1086/321449](https://doi.org/10.1086/321449)
- Migliari, S., Fender, R.P., Rupen, M, et al., 2003, MNRAS, 342, 67.
- Migliari, S., & Fender, R. P. 2006, MNRAS, 366, 79, doi: [10.1111/j.1365-2966.2005.09777.x](https://doi.org/10.1111/j.1365-2966.2005.09777.x)
- Migliari, S., Miller-Jones, J. C. A., Fender, R. P., et al. 2007, ApJ, 671, 706, doi: [10.1086/522516](https://doi.org/10.1086/522516)
- Mirabel, I. F. 1993, La Recherche, 255, 746
- Muzerolle, J., Flaherty, K., Balog, Z., Beck, T., & Gutermuth, R. 2019, ApJ, 877, 29, doi: [10.3847/1538-4357/ab1756](https://doi.org/10.3847/1538-4357/ab1756)
- Nowak, M., Wilms, J., Pottschmidt, K., et al. 2011, HEAD 12.0107N.
- Papitto, A., Ferrigno, C., Bozzo, E. et al., 2013, Nature, 501, 517.
- Phillipson, R.A., Boyd, P.T., and Smale, A.P., 2018, MNRAS, 477, 5220.
- Plotkin, R. M., Gallo, E., & Jonker, P. G. 2013, ApJ, 773, 59, doi: [10.1088/0004-637X/773/1/59](https://doi.org/10.1088/0004-637X/773/1/59)
- Pradhan, P., Maitra, C., Paul, B., 2020, ApJ, 895, id. 10P.
- Remillard, R. A., & McClintock, J. E. 2006, ARA&A, 44, 49, doi: [10.1146/annurev.astro.44.051905.092532](https://doi.org/10.1146/annurev.astro.44.051905.092532)
- Roming, P. W. A., Kennedy, T. E., Mason, K. O., et al. 2005, SSRv, 120, 95, doi: [10.1007/s11214-005-5095-4](https://doi.org/10.1007/s11214-005-5095-4)
- Saavedra, E.A., Sosomayor, C.P., Vieyro, F.L., and Romero, G.E., 2022, Boletín de la Asociación Argentina de Astronomía, 63, 274.
- Sasano, M., Makishima, K., Sakurai, S., Zhang, Z., and Enoto, T., 2014, PASJ, 66, id.35s.
- Sault, R. J., Engel, C., & de Pater, I. 2004, Icarus, 168, 336, doi: [10.1016/j.icarus.2003.11.014](https://doi.org/10.1016/j.icarus.2003.11.014)
- Sault, R.J., Teuben, P.J., and Wright, M.C.H., 1995, Astronomical Data Analysis Software and Systems IV, ASP Conference Series, Vol. 77, R.A. Shaw, H.E. Payne, and J.J.E. Hayes, eds., p. 433.
- Schulz, N.S., Kallman, T.E., Heinz, S., et al., 2020, ApJ, 891, id. 150S.
- Shaw, A. W., Plotkin, R. M., Miller-Jones, J. C. A., et al. 2021, ApJ, 907, 34, doi: [10.3847/1538-4357/abd1de](https://doi.org/10.3847/1538-4357/abd1de)
- Shidatsu, M., Ueda, Y., Tazaki, F., et al. 2011, PASJ, 63, S785, doi: [10.1093/pasj/63.sp3.S785](https://doi.org/10.1093/pasj/63.sp3.S785)
- Sivakoff, G., Russell, D., Markoff, S., et al. 2016, in 41st COSPAR Scientific Assembly, Vol. 41, E1.6–4–16
- Strohmayer, T.E. and Markwardt, C.B., 2002, ApJ, 577, 337.
- Tetarenko, A.J., Rosolowsky, E.W., Miller-Jones, J.C.A., and Sivakoff, G.R., 2020, MNRAS, 497, 3504.
- van den Eijnden, J., Degenaar, N., Russell, T. D., et al. 2018, Nature, 562, 233, doi: [10.1038/s41586-018-0524-1](https://doi.org/10.1038/s41586-018-0524-1)
- van der Walt, S., Colbert, S. C., & Varoquaux, G. 2011, Computing in Science and Engineering, 13, 22, doi: [10.1109/MCSE.2011.37](https://doi.org/10.1109/MCSE.2011.37)
- Virtanen, P., Gommers, R., Oliphant, T. E., et al. 2020, Nature Methods, 17, 261, doi: [10.1038/s41592-019-0686-2](https://doi.org/10.1038/s41592-019-0686-2)
- Vrtillek, S. D., & Boroson, B. S. 2013, MNRAS, 428, 3693, doi: [10.1093/mnras/sts312](https://doi.org/10.1093/mnras/sts312)
- Vrtillek, S. D., Raymond, J. C., Boroson, B., et al. 2001, ApJL, 563, L139, doi: [10.1086/338733](https://doi.org/10.1086/338733)

Yu, W. and Dolence, J., 2007, ApJ, 667, 1043Y.

in't Zand, J.J.M., Kuulkers, E., Verbunt, F., et al, 2003,
A&A, 411, L487.

APPENDIX

A. ASM 14-YEAR LIGHTCURVES

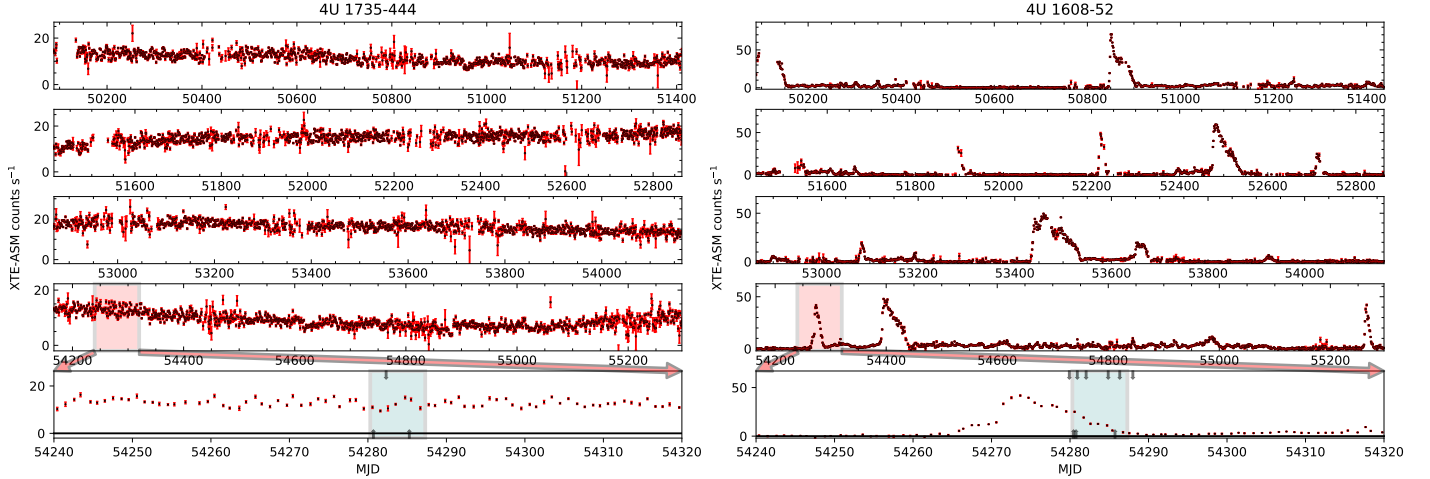
Fig. Set 32. RXTE-ASM Lightcurves

Figure 32. X-ray light curves for two sample XRBs with data from the RXTE ASM. The upper four rows show the X-ray flux in counts per second for most of the lifetime of the instrument ($50100 < \text{MJD} < 55300$, i.e. January 1996 through April 2010). The bottom row is an expanded scale view of the 80 days surrounding our observing campaign, highlighted in pink on the fourth row above. The seven days of the campaign are highlighted in blue. Markers on the top scale of the bottom panel indicate the times of observations with the Swift XRT (Table 6). Markers on the bottom scale indicate times of observations with the RXTE PCA (Tables 9 and 10), or the end points of the range in cases where all observations were averaged together. Error bars on the daily averages are drawn in red. The complete figure set (42 images) is available in the online journal.

Fig. 32 and the associated figure set shows RXTE All Sky Monitor lightcurves of 42 of the sources in this study for most of the fifteen years that the RXTE was active. They illustrate the variability type of the object. For example: 4U 1735-44 is a persistent source and 4U1608-52 is a transient source with accretion disk outbursts. The 80 day interval around the week of the 2007 campaign is expanded in the bottom panel to emphasize the context of the source luminosity variation during our observations. For example, 4U1608-52 was in the downward side of an accretion disk outburst whereas 4U 1735-44 was varying around its typical flux density during our campaign. The y axis is flux density in counts per second summed over the three ASM bands 1.3 - 12 keV. As discussed by [Vrtilek & Boroson \(2013\)](#), the last two years of ASM operation showed gradually more frequent gain variations that were not present in the earlier 14 years. Thus we cut off the lightcurves at about $\text{MJD}=55300$, nearly three years after our observing campaign.